The TESS-Keck Survey. XV. Precise Properties of 108 TESS Planets and Their Host Stars

Mason G. MacDougall[1], Erik A. Petigura[1], Gregory J. Gilbert[1], Isabel Angelo[1], Natalie M. Batalha[2], Corey Beard[3], Aida Behmard[4,19], Sarah Blunt[5,19], Casey Brinkman[6,19], Ashley Chontos[6,7,20], Ian J. M. Crossfield[8], Fei Dai[4], Paul A. Dalba[2,9,21], Courtney Dressing[10], Tara Fetherolf[11,22], Benjamin Fulton[12], Steven Giacalone[10], Michelle L. Hill[11], Rae Holcomb[3], Andrew W. Howard[5], Daniel Huber[6], Howard Isaacson[10,13], Stephen R. Kane[11], Molly Kosiarek[2], Jack Lubin[3], Andrew Mayo[10], Teo Močnik[14], Joseph M. Akana Murphy[2,19], Daria Pidhorodetska[11], Alex S. Polanski[8], Malena Rice[15,19], Paul Robertson[3], Lee J. Rosenthal[5], Arpita Roy[16,17], Ryan A. Rubenzahl[5,19], Nicholas Scarsdale[2], Emma V. Turtelboom[10], Dakotah Tyler[1], Judah Van Zandt[1], Lauren M. Weiss[18], and Samuel W. Yee[7]

[1] Department of Physics & Astronomy, University of California, Los Angeles, Los Angeles, CA 90095, USA; macdougall@astro.ucla.edu
[2] Department of Astronomy and Astrophysics, University of California, Santa Cruz, Santa Cruz, CA 95060, USA
[3] Department of Physics & Astronomy, University of California, Irvine, Irvine, CA 92697, USA
[4] Division of Geological and Planetary Science, California Institute of Technology, Pasadena, CA 91125, USA
[5] Department of Astronomy, California Institute of Technology, Pasadena, CA 91125, USA
[6] Institute for Astronomy, University of Hawaiʻi, Honolulu, HI 96822, USA
[7] Department of Astrophysical Sciences, 4 Ivy Lane, Princeton University, Princeton, NJ 08544 USA
[8] Department of Physics & Astronomy, University of Kansas, Lawrence, KS 66045, USA
[9] SETI Institute, Carl Sagan Center, 339 Bernardo Ave., Suite 200, Mountain View, CA 94043, USA
[10] Department of Astronomy, University of California, Berkeley, Berkeley, CA 94720, USA
[11] Department of Earth and Planetary Sciences, University of California, Riverside, Riverside, CA 92521, USA
[12] NASA Exoplanet Science Institute/Caltech-IPAC, Pasadena, CA 91125, USA
[13] Centre for Astrophysics, University of Southern Queensland, Toowoomba, QLD, Australia
[14] Gemini Observatory/NSF's NOIRLab, 670 N. A'ohoku Place, Hilo, HI 96720, USA
[15] Department of Astronomy, Yale University, New Haven, CT 06520, USA
[16] Space Telescope Science Institute, Baltimore, MD 21218, USA
[17] Department of Physics and Astronomy, Johns Hopkins University, Baltimore, MD 21218, USA
[18] Department of Physics and Astronomy, University of Notre Dame, Notre Dame, IN 46556, USA

Abstract

We present the stellar and planetary properties for 85 TESS Objects of Interest (TOIs) hosting 108 planet candidates that compose the TESS-Keck Survey (TKS) sample. We combine photometry, high-resolution spectroscopy, and Gaia parallaxes to measure precise and accurate stellar properties. We then use these parameters as inputs to a light-curve processing pipeline to recover planetary signals and homogeneously fit their transit properties. Among these transit fits, we detect significant transit-timing variations among at least three multiplanet systems (TOI-1136, TOI-1246, TOI-1339) and at least one single-planet system (TOI-1279). We also reduce the uncertainties on planet-to-star radius ratios $R_p/R_\star$ across our sample, from a median fractional uncertainty of 8.8% among the original TOI Catalog values to 3.0% among our updated results. With this improvement, we are able to recover the Radius Gap among small TKS planets and find that the topology of the Radius Gap among our sample is broadly consistent with that measured among Kepler planets. The stellar and planetary properties presented here will facilitate follow-up investigations of both individual TOIs and broader trends in planet properties, system dynamics, and the evolution of planetary systems.

1. Introduction

The NASA Transiting Exoplanet Survey Satellite (TESS; Ricker et al. 2015) is currently in its fifth year of carrying out an all-sky survey in search of transiting planets orbiting nearby bright stars. So far, TESS has revealed over 6000 planet candidates, building on the legacies of its predecessors, NASA's Kepler (Borucki et al. 2010) and K2 (Howell et al. 2014). These TESS Objects of Interest (TOIs) are now the subjects of numerous follow-up studies to verify their planetary nature and measure their properties (e.g., Kane et al. 2021; Teske et al. 2021; Chontos et al. 2022; Yee et al. 2022). The precise characterization of planet properties, however, is greatly dependent on the robustness of the input stellar parameters and light-curve modeling procedure.

The TESS Input Catalog (TIC; Stassun et al. 2018; ExoFOP 2019; Stassun et al. 2019) contains stellar parameters for all TESS targets that were measured from broadband

photometry and parallaxes. These stellar properties were used as inputs to the TESS data processing pipeline developed by the Science Processing Operations Center (SPOC; Jenkins et al. 2016), which flags planet candidates as TOIs and performs an initial characterization (Guerrero et al. 2021; NASA Exoplanet Archive 2022). The propagation of large uncertainties throughout this process can lead to miscalculated or poorly constrained planet radii for TOIs, with a median fractional radius uncertainty of $\sigma(R_p)/R_p \approx 7.4\%$ and a mean fractional uncertainty of $\sim 20.2\%$. This large discrepancy between the median and mean uncertainty is due to a significant high-$\sigma(R_p)$ tail, with roughly one in five TOIs having $\sigma(R_p)/R_p > 20\%$.

The TESS-Keck Survey (TKS) has set out to confirm and characterize a sample of 108 TOIs orbiting 85 TESS host stars (Chontos et al. 2022). The TKS Collaboration aims to precisely measure the stellar properties of this sample using spectra taken with the High-Resolution Spectrograph (HIRES; Vogt et al. 1994) on the Keck I telescope at the W. M. Keck Observatory. These spectra also allow us to dynamically confirm the planetary nature of the TKS TOIs through the measurement of precise radial velocities (RVs), leading to numerous planet discoveries among the TKS team (e.g., Dai et al. 2020; Dalba et al. 2020; MacDougall et al. 2021; Rubenzahl et al. 2021; Scarsdale et al. 2021; Weiss et al. 2021; Dalba et al. 2022; Lubin et al. 2022; MacDougall et al. 2022; Turtelboom et al. 2022; Van Zandt et al. 2023).

To ensure consistency among the planetary and stellar parameters reported for TKS targets, we use the stellar parameters measured with our spectroscopic constraints as inputs to a light-curve detrending and transit fitting pipeline applied homogeneously to all TKS targets. The planet properties derived by our pipeline allow us to begin addressing the major TKS Science Cases (see Chontos et al. 2022), such as improving our understanding of planet bulk compositions, system architectures and dynamics, planetary atmospheres, and the role of stellar evolution in shaping planetary systems.

In this work, we describe our homogeneous characterization of both planetary and stellar properties of TKS targets, derived from transit photometry and single stellar spectra. In Section 2, we update the stellar properties reported by Chontos et al. (2022) with additional photometric constraints and compare these results against those reported by the TOI Catalog and Gaia Data Release 2. We also derive estimates of the quadratic limb-darkening parameters for each TOI host to set priors on our transit model. In Section 3, we describe the data processing pipeline used to retrieve, detrend, and fit the light-curve photometry for our target sample. We account for both stellar variability and transit-timing variations (TTVs) in order to properly model the transit signals. We use the results from our transit fits and stellar characterization to derive various planet parameters in Section 4, including planet radius, which we measure to a median uncertainty of 3.8%. In Section 5, we offer some preliminary insight gained through this analysis to begin addressing the science goals of TKS, which will be evaluated in more depth in future works by the TKS team. Planet masses, precise eccentricities, and nontransiting companions are not addressed in this transit-focused study, and we leave that analysis to a full RV analysis by TKS collaborators (A. Polanski et al. 2023, in preparation).

2. Stellar Properties

2.1. Spectroscopic Constraints

The TKS Collaboration has collected spectra for the 85 TOIs from Chontos et al. (2022) at a spectral resolution of $R = 50,000$ using the HIRES instrument at the W. M. Keck Observatory (Vogt et al. 1994) from Summer 2019 to Fall 2022. We used iodine-free reconnaissance spectra, with signal-to-noise ratio (S/N) $\approx 40\,\mathrm{pixel}^{-1}$ across 3600–9000 Å, to check for rapid stellar rotation and rule out spectroscopic false positives. We also extracted stellar effective temperature T_{eff}, metallicity [Fe/H], and surface gravity log$g$ from these spectra using two different methods according to the estimated effective temperature per target. The two methods used were SpecMatch-Syn (synthetic; Petigura 2015) and Spec-Match-Emp (empirical; Yee et al. 2017). SpecMatch-Syn compares a given stellar spectrum to synthetic spectra generated by interpolating within a grid of modeled spectra from a library described by Coelho et al. (2005). Spec-Match-Emp fits a stellar spectrum via direct comparison to observed optical spectra from a dense library of stars with well-measured properties.

We initially processed the spectra of each target using both techniques and used their respective valid ranges of effective temperature to determine which set of derived properties is more reliable for a given star. Specifically, we use Spec-Match-Syn measurements for stars with estimated effective temperature between 4800 and 6500 K, as determined by SpecMatch-Emp. For stars with estimated T_{eff} beyond this range (i.e., $T_{\mathrm{eff}} < 4800$ K and $T_{\mathrm{eff}} > 6500$ K), we use SpecMatch-Emp measurements. In cases where Spec-Match-Emp is used, the SpecMatch model does not output an estimate of log$g$.

2.2. Isochrone Modeling

2.2.1. Input Values

We derive additional stellar properties such as mass $M_\star$, radius $R_\star$, density $\rho_\star$, luminosity $L_\star$, age, and extinction A_v using isoclassify (Huber et al. 2017; Berger et al. 2020a). This software interpolates between the MESA Isochrones and Stellar Tracks (MIST) models (Choi et al. 2016; Dotter 2016) to measure the best-fitting solution of stellar properties for a given set of input spectroscopic and photometric constraints. For M dwarfs, isoclassify uses empirical relations from Mann et al. (2019) to derive fundamental stellar properties (see Berger et al. 2020a for details). isoclassify has been shown to produce robust results and was the foundation for deriving the Gaia-Kepler stellar properties catalog (Berger et al. 2020a).

We used the outputs of the preferred SpecMatch model per target as priors to constrain the isochrone grid space explored by our isoclassify models. This includes priors on T_{eff} and [Fe/H] from either SpecMatch method, along with a prior on log$g$ when SpecMatch-Syn is preferred. We also include priors on stellar parallax drawn from Gaia DR2, with a median uncertainty of 0.03 mas. We incorporate photometric inputs for several all-sky photometric bands from the Two Micron All Sky Survey (2MASS; Skrutskie et al. 2006) and Gaia missions to further constrain our isoclassify results. These bands are 2MASS J, H, K and Gaia DR2 G, B_p, R_p, from which various photometric colors are used to calibrate the
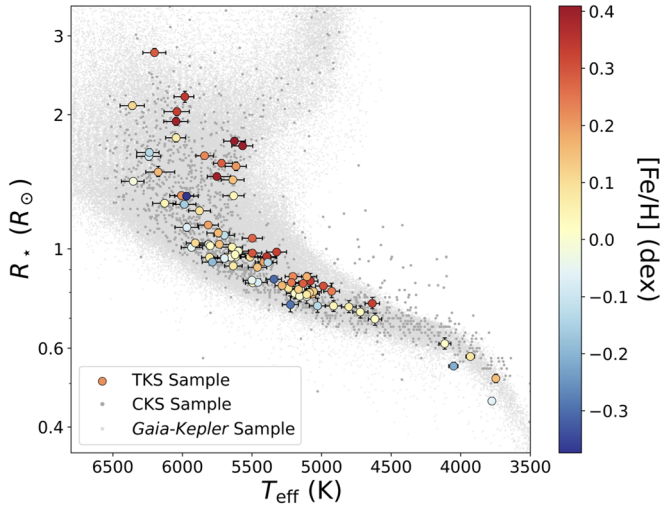
Figure 1. Stellar radius as a function of effective temperature for the 85 host stars in the TKS sample, with metallicity shown as color gradient. The CKS sample (Petigura et al. 2022) and the Gaia-Kepler sample (Berger et al. 2020a, 2020b) are shown for reference in dark and light gray, respectively.

Table 1
Median Fractional Uncertainties

	Parameter	TKS Result Unc. (%)	TOI Catalog Unc. (%)
Star	$R_\star$	1.7	5.1
	$M_\star$	3.0	12.6
	$T_{\rm eff}$	1.2	2.3
	$\log g$	0.52	1.9
Planet	R_p	3.8	6.7
	$R_p/R_\star$	3.0	8.8
	T_{14}	1.8	9.7
	P	2.2×10^{-4}	3.8×10^{-4}
	t_0	7.1×10^{-5}	7.3×10^{-5}

Note. Reported fractional uncertainties for several stellar and planetary parameters compared between our TKS results and those reported in the TOI Catalog, demonstrating our improved precision across the TKS sample. The values presented here do not account for systematic uncertainties that may arise from differences in underlying stellar model grids (see Section 2.2.2).

underlying isochrone model grid. We also select 2MASS K as the photometric band to be used for absolute magnitude calculations during `isoclassify` modeling. All input parameter priors are assumed to be normally distributed.

The inclusion of multiple photometric constraints allows us to fit for extinction directly using `isoclassify` without needing to specify a generalized dust map (see, e.g., Lallement et al. 2019), making our extinction and metallicity estimates more accurate on a target-by-target basis. This improves the accuracy of our stellar characterizations as compared to Chontos et al. (2022), where only a single photometric band was used with a generalized dust map. The median uncertainty for the 2MASS photometry that we use is 0.02 mag. To account for systematic zero-point differences in photometric systems, we use a standardized uncertainty floor of 0.01 mag for Gaia photometry.

With these inputs to `isoclassify`, we perform stellar characterization via isochrone grid modeling to measure $M_\star$, $R_\star$, $\rho_\star$, $L_\star$, age, and A_v for all 85 TKS targets, in addition to spectroscopically constrained $T_{\rm eff}$, [Fe/H], and $\log g$. This catalog of precise homogeneously derived stellar properties will serve as a reference for all future TKS studies and as a resource for the broader astronomy community. We show the relationship between $R_\star$–$T_{\rm eff}$–[Fe/H] in Figure 1 for this sample, as compared to the distributions of both the California-Kepler Survey (CKS) sample (Petigura et al. 2017b) and the Gaia-Kepler sample (Berger et al. 2020a 2020b). We note that the TKS sample includes a broad range of stellar types, similar to the distributions of stars studied of similar past works.

2.2.2. Uncertainties

The median uncertainties that we measure for $R_\star$, $M_\star$, $T_{\rm eff}$, and $\log g$ are reported in Table 1, as compared against the original TOI Catalog source uncertainties (Guerrero et al. 2021; NASA Exoplanet Archive 2022). We do not currently account for model-dependent uncertainties associated with the MIST models to maintain consistency with the reported uncertainties by the TOI Catalog and Gaia DR2 catalog. The appropriate corrections (described by Tayar et al. 2022) can be added in quadrature to our error values to encapsulate this systematic

error. When we perform this correction, we find updated median fractional uncertainties of 4.5%, 4.0%, 1.3%, and 0.6% for $R_\star$, $M_\star$, $T_{\rm eff}$, and $\log g$, respectively. Most notable among these is the change in the stellar radius uncertainty, which increased from 1.7% to 4.5% when the systematic error was introduced. This ultimately propagates to an increase in the median R_p uncertainty as well, from 3.8% to 5.8%. Even with this additional systematic uncertainty on R_p, our results remain better constrained compared to the TOI Catalog.

We also note that two targets from the TKS sample have missing or erroneous 2MASS catalog uncertainties. TOI-1807 has an anomalously large K-mag uncertainty ($\sigma_K = 10$ mag), and TOI-1246 is missing an uncertainty value for J-mag. We replaced both of these with a standardized uncertainty value of 0.02 mag, roughly consistent with the median errors for these bands among our sample.

2.2.3. Comparison with TOI Catalog and Gaia Results

To validate our stellar parameters, we compared our final values of $T_{\rm eff}$ and $R_\star$ from `isoclassify` with the TOI Catalog and Gaia DR2. We show these comparisons in Figure 2. The stellar parameters measured from these external sources were calculated using either photometry with parallaxes (TOI Catalog; Stassun et al. 2018) or a combination of photometry with parallaxes and low-resolution spectra (Gaia DR2; Bailer-Jones et al. 2013).

For each comparison, we calculated the ratio of the given parameter between our TKS results and the external source data (i.e., $R_{\star,\rm TKS}/R_{\star,\rm TOI}$) to demonstrate the lack of bias in these results. We measured the mean and standard deviation of these ratio distributions for each comparison and found the following: (Figure 2(a)) $R_{\star,\rm TKS}/R_{\star,\rm Gaia} = 0.99 \pm 0.04$, (Figure 2(b)) $T_{\rm eff,TKS}/T_{\rm eff,Gaia} = 1.00 \pm 0.01$, (Figure 2(c)) $R_{\star,\rm TKS}/R_{\star,\rm TOI} = 0.99 \pm 0.03$, and (Figure 2(d)) $T_{\rm eff,TKS}/T_{\rm eff,TOI} = 1.00 \pm 0.02$. The scatter between our TKS results and the external data source for each comparison was consistent with the reported parameter uncertainty. This implies a general agreement between our TKS stellar parameters and those reported by external data sources. We do find that the Gaia DR2 pipeline produces overestimated $T_{\rm eff}$ for cooler TKS stars, but this is consistent with a known degradation in the
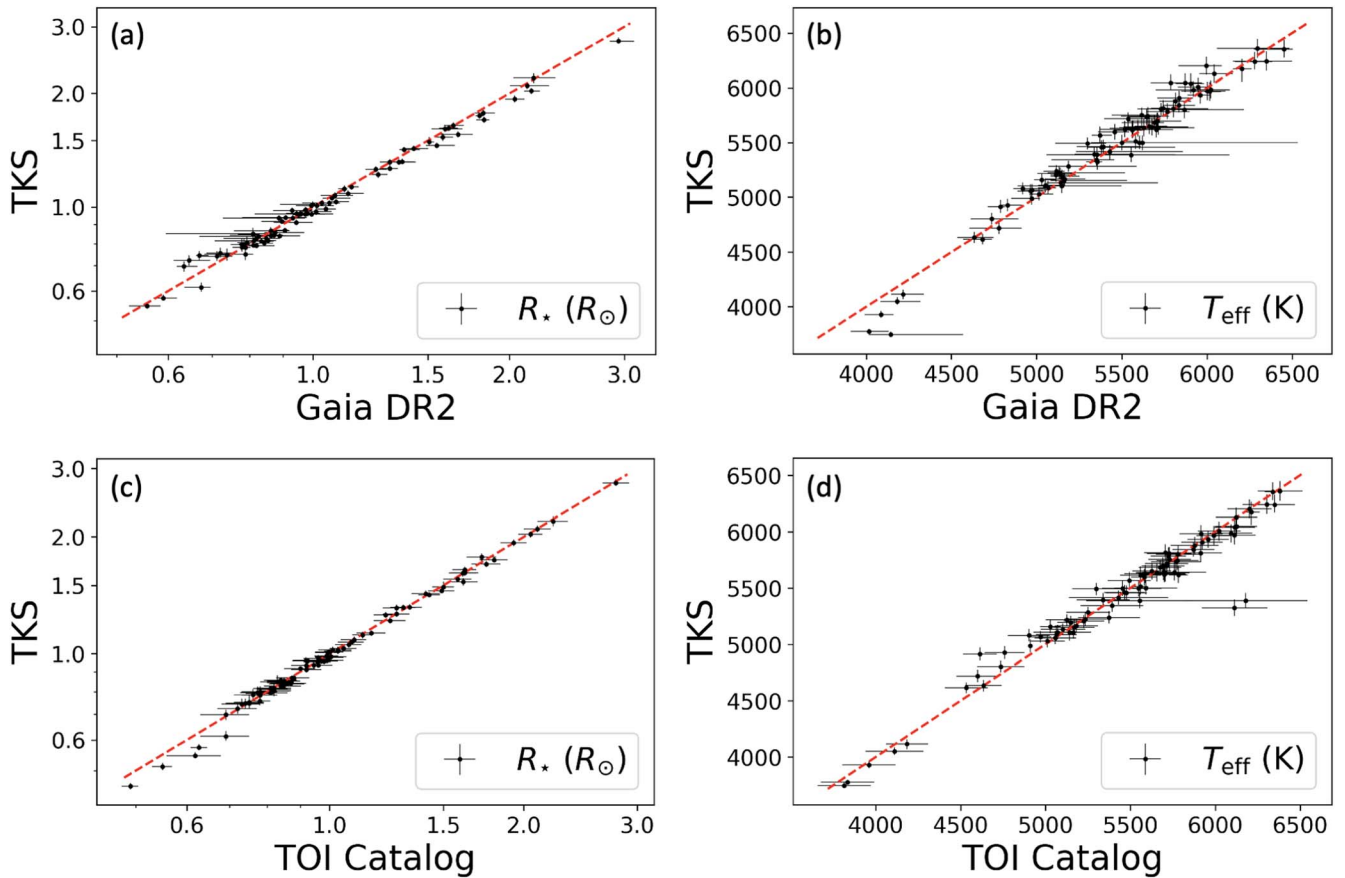
Figure 2. Stellar radius (left) and effective temperature (right) as measured by our stellar characterization procedure (TKS) on the y-axis compared to the values reported by the Gaia DR2 pipeline (top) and the TOI Catalog (bottom) on the x-axis. The TKS results produce reduced uncertainties and are generally consistent with one or both external sources. The residuals of our comparison between $R_{\star,\mathrm{TKS}}$ and $R_{\star,\mathrm{TOI}}$ can be seen in Figure 6(a). We also note that the Gaia DR2 pipeline does not report stellar properties when $R_{\star,\mathrm{Gaia}} \lesssim 0.5\ R_\odot$, leaving out two TKS targets.

precision of the Gaia DR2 pipeline around $T_{\mathrm{eff}} \approx 4000$ K (Andrae et al. 2018).

From these comparisons, we flag two targets with discrepancies of $>3\sigma$ between our results and the values reported from the external data sources. TOI-2145 had an estimated effective temperature whose uncertainty spanned across the threshold of reliability between SpecMatch-Emp and SpecMatch-Syn. Selecting between these two methods following the criteria in Section 2.1 yielded a radius measurement for this target that was inconsistent with both the TOI Catalog and Gaia DR2 estimates. By manually swapping methods and allowing for an exception to these rules, we found good alignment between our final radius measurement and the values reported from the other two sources. The remaining flagged target (TOI-2114), which can be seen in Figure 2(d), has a discrepant T_{eff} when we compare our result to the TOI Catalog. However, our result remains highly consistent with the T_{eff} reported by Gaia DR2 and other external sources. Given this observation and the relatively large uncertainties reported by the TOI Catalog, we attribute the disagreement to slight differences in modeling methods and proceed without making any adjustments for this particular target.

2.3. Limb Darkening

Stellar limb darkening is the decrease in brightness of the disk of the star from its center toward its edge or limb. A set of

quadratic coefficients is often used to define this limb-darkening function, which describes the ingress and egress of a transit profile (Mandel & Agol 2002). An accurate estimate of limb-darkening coefficients is crucial for measuring accurate planet properties, especially for planets that transit closer to the limb of a star (e.g., higher impact parameter or inclination).

There are two leading stellar atmosphere models that are widely used for calculating quadratic limb-darkening coefficients: the PHOENIX model (Hauschildt & Baron 1999) as implemented by Husser et al. (2013), and the ATLAS models (Castelli & Kurucz 2003) as implemented by Claret & Bloemen (2011). Investigations into the accuracy of these two methods (see, e.g., Patel & Espinoza 2022) have demonstrated that such models produce quadratic limb-darkening coefficients with an average discrepancy of $\sim$0.1. For reference, a typical quadratic limb-darkening value for a solar-like star is in the range 0.1–0.5, so an uncertainty of 0.1 is typically $>$20% of the nominal measurement. Additionally, this formal uncertainty between methods only encompasses part of the true uncertainty that arises when measuring these coefficients from atmospheric models. With this in mind, we use the limb-darkening code (Espinoza & Jordán 2015) to easily compute both the PHOENIX-derived and ATLAS-derived limb-darkening coefficients for all targets in our sample. This derivation requires several stellar inputs, which we draw from our isoclassify results: T_{eff}, [Fe/H], and log$g$. We then use these values to adopt nominal estimates of coefficients $\{u_1, u_2\}$ for each target with a systematic noise floor of 0.1.
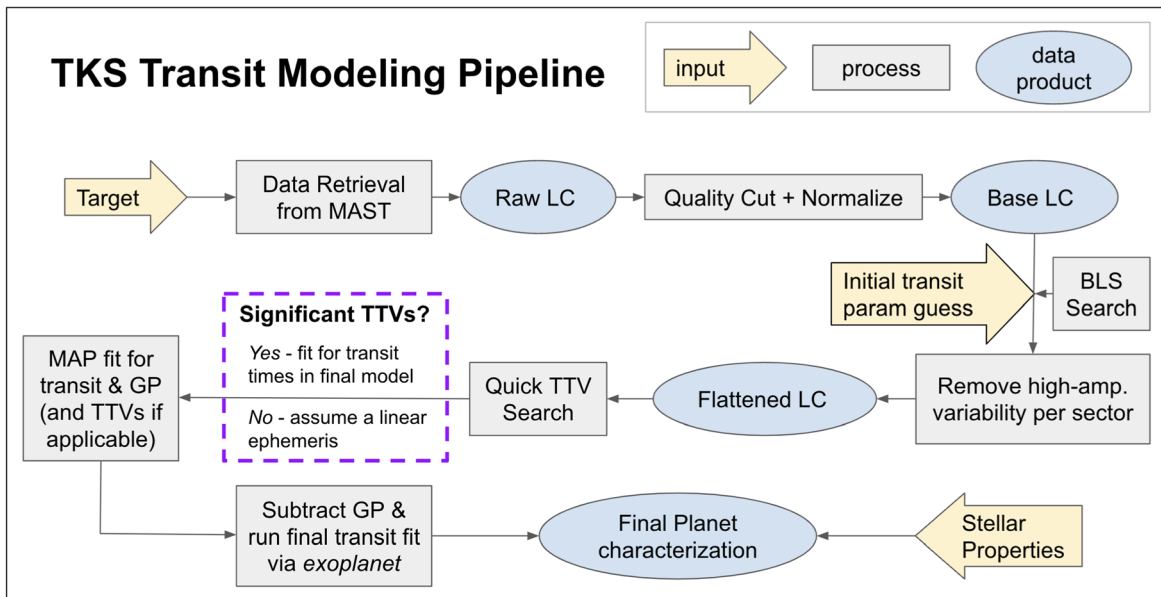
Figure 3. Diagram demonstrating the flow of data throughout the TKS light-curve modeling pipeline. Yellow arrows are data inputs, gray boxes are processes, and blue ovals are data products.

Given the large uncertainty in these measurements, we establish a simple set of rules to determine which set of limb-darkening coefficients (u_i) to use in deriving our final catalog of system properties: (1) When $|u_{i,\mathrm{ATLAS}} - u_{i,\mathrm{PHOENIX}}| < 0.1$, we select $\mathrm{AVG}(u_{i,\mathrm{ATLAS}}, u_{i,\mathrm{PHOENIX}})$ as the final coefficient values. (2) When $|u_{i,\mathrm{ATLAS}} - u_{i,\mathrm{PHOENIX}}| \geqslant 0.1$, we select $u_{i,\mathrm{ATLAS}}$ as the final coefficient values. These rules were established upon consideration of the systematic comparison of these two methods carried out by Patel & Espinoza (2022). We also assume a standardized uncertainty of 0.1 for all limb-darkening coefficients among the TKS sample, which is later propagated into a model prior during our transit fitting procedure.

3. Light-curve Modeling

3.1. Input Data

We perform our light-curve detrending and modeling using transit photometry from Sectors 1–60 of the TESS mission. We accessed the Pre-search Data Conditioning Simple Aperture Photometry (PDC-SAP; Smith et al. 2012; Stumpe et al. 2012, 2014) through the Mikulski Archive for Space Telescopes (MAST). For the majority of TKS targets, we used 2-minute-cadence time-series photometry processed by the primary TESS Science Processing Operations Center pipeline (SPOC; Jenkins et al. 2016). For TOI-1386, TOI-1601, and TOI-2045, photometry from the primary SPOC pipeline was unavailable, so we instead used PDC-SAP photometry from the TESS-SPOC updated pipeline, which produces light curves for targets selected from full-frame image observations (Caldwell et al. 2020).

3.2. False-positive Vetting

While false-positive vetting is not a primary focus of this work, we acknowledge that the resolved false-positive rate among *all* TOIs is on the order of ∼20%–30% (Cacciapuoti et al. 2022; NASA Exoplanet Archive 2022; Magliano et al. 2023). However, this is an extreme upper bound for the TKS sample. We specifically selected our sample to include *only*

TOIs with unambiguous planetary dispositions confirmed by both the initial TOI vetting pipeline (Guerrero et al. 2021) and the TESS Follow-up Program Working Group.

Additionally, all TKS targets were individually vetted by members of the TKS Collaboration, as detailed in Chontos et al. (2022). This vetting process allowed us to establish a set of selection rules to minimize the risk of including unresolved false positives in our final target sample by making cuts based on transit S/N, out-of-transit centroid offsets, and the proximity of stellar companions. Therefore, we suspect that the false-positive rate in the TKS sample is much lower than the quoted upper bound, but we leave a quantitative assessment of this value for later work. Should any of the TKS TOIs be deemed false positives, the planetary properties presented here would need to be revisited.

3.3. Light-curve Preprocessing

We apply the following preprocessing routine homogeneously across all light curves for the 85 TKS targets. A complete outline of this preprocessing routine and our subsequent modeling pipeline can be found in a flowchart in Figure 3. We first mask all points that were flagged for poor quality (quality flag > 0), with the exception of TOI-1456, for which a valid transit signal is mistakenly flagged as scattered light contamination by the SPOC pipeline (see Dalba et al. 2020). We then normalize each light-curve sector iteratively and subtract 1 from the normalized flux values such that $\mu_{\mathrm{flux}} = 0$ for all sectors. We also flag four light curves as having high stellar variability, which we determine based on whether or not the standard deviation of a target's out-of-transit flux is $>3\sigma_{\mathrm{flux}}$, where σ_{flux} is the median uncertainty of the individual photometric data points. These four targets are TOI-1136, TOI-1726, TOI-1807, and TOI-2076. We also apply an upper sigma cut of 5σ to remove high photometric outliers among targets that do not meet this high-variability criterion.

For light curves with low stellar variability, we perform a box least-squares (BLS; Kovács et al. 2002) search to determine initial estimates of the orbital period and first transit
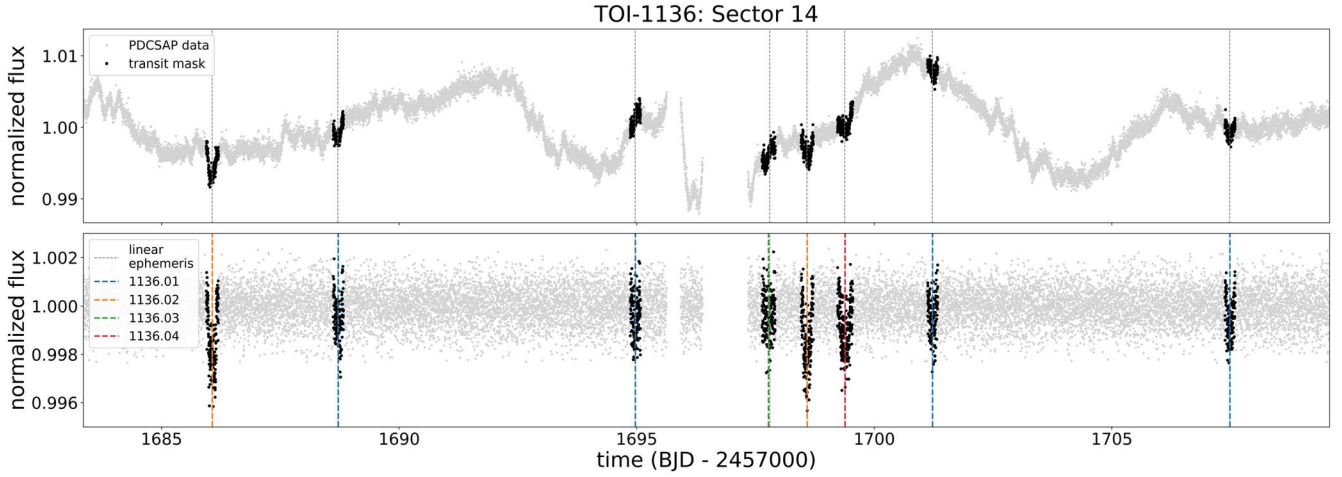
Figure 4. Before (top) and after (bottom) applying our detrending and initial TTV fitting procedure to the photometry of TOI-1136, a multiplanet system with high stellar variability. We only show the first sector (Sector 14) of this target's photometry here, but all sectors display similar variability. We model our detrended transit photometry and measure $R_p/R_\star$ values for all four planets that agree with the values reported by Dai et al. (2023) within $\sim 1.5\sigma$, as opposed to the TOI Catalog values, which are all more than 1.5σ discrepant. Black points highlight transits (± 0.75 times T_{14}), colored vertical dashed lines show modeled transit midpoints, and dark-gray vertical dashed lines show calculated transit midpoints assuming a linear ephemeris. In the sector shown, we find the most significant TTVs for TOI-1136.03 (green) as can be seen by the separation between the modeled and calculated midpoints.

midpoint of each planet. We compare the BLS search results to estimates taken from the primary TOI Catalog (NASA Exoplanet Archive 2022), flagging any results with $>3\sigma$ discrepancy when compared to this source. We then follow up flagged targets with a manual inspection, determining that all discrepancies are likely the result of new photometry assisting in pinning down the orbital period with greater precision. In cases of high stellar variability, we do not perform this initial BLS search and instead proceed with the values drawn directly from the TOI Catalog or other literature as our initial guesses.

We use these period and midpoint values, along with transit durations from the TOI catalog, to mask out all transits with a mask width of ± 0.75 times the transit duration from the transit midpoint. While this mask does not yet account for TTVs, we use it here for an initial detrending step, which we improve on in our subsequent fit in Section 3.5. With the masked photometry, we modeled stellar variability in each light-curve sector using a Gaussian process (GP) via celerite2 (Foreman-Mackey 2018) through the exoplanet interface (Foreman-Mackey et al. 2021). The GP fit includes a term to model the variability via a stochastically driven damped harmonic oscillator with quality factor $Q = 1/\sqrt{2}$, with lognormal priors on both the undamped period (ρ_{GP}) and the standard deviation of the process (σ_{GP}) with means $\mu_{\rho_{\mathrm{GP}}} = 0$ and $\mu_{\sigma_{\mathrm{GP}}} = \ln(\sigma_{\mathrm{flux}})$, respectively. We interpolate over the masked transits to create a smooth fit to the variability for each light-curve sector and subtract this trend from the original unmasked data to produce an initial flattened light curve. We stitch together the flattened photometry for each sector and save the maximum a posteriori (MAP) parameters for the GP fit, which we use later as informed initial guesses in a more complete light-curve model.

3.4. Estimating TTVs

Along with determining an initial fit to the stellar variability trend, we also use the exoplanet light-curve modeling package to find an initial MAP fit to the transit times for each planet. We use our previous P and t_0 estimates to calculate a set of initial guesses for the transit times assuming a linear

Table 2
Transit Model Priors

Parameter	Prior
P (days)	$\log P \sim N(\log P_{\mathrm{init}}, 1)$
t_0 (days)	$t_0 \sim N(t_{0,\mathrm{init}}, 1)$
$R_p/R_\star$	$\log(R_p/R_\star) \sim U(-9, 0)$
b	$b \sim U(0, 1 + R_p/R_\star)$
T_{14} (days)	$\log T_{14} \sim U(-9, 0)$
u_i	$u_i \sim N(u_{i,\mathrm{init}}, 0.1)$
μ	$\mu \sim N(0, 1)$
σ_{LC}	$\log \sigma_{\mathrm{LC}} \sim N(\log \sigma_{\mathrm{flux}}, 1.0)$

Note. Priors on final transit model parameters. P, T_{14}, and t_0 are all given in units of days, with t_0 using the reference frame BJD $-2,457,000$. Priors include normal (N) and uniform (U) distributions.

ephemeris. We model the true transit times for each planet using an initial Gaussian prior for each transit time, centered on their linear ephemeris values with a standard deviation of 0.1 days. Along with the transit times, we also fit the planet-to-star radius ratio ($R_p/R_\star$), impact parameter (b), transit duration from first to fourth contact (T_{14}), quadratic limb-darkening parameters (u_1, u_2), mean out-of-transit flux (μ), and light-curve jitter (σ_{LC}). The orbital period (P) and initial transit midpoint (t_0) are also measured as derived values. The priors used on all modeled parameters are given in Table 2 and described in more detail in Section 3.5.

This MAP fit to the transit shape and transit times allows us to get a quick estimate of any TTVs detected for each planet. Based on these estimates, we determine for each planet whether to proceed with a final model that assumes a linear ephemeris or includes transit-time fits with a Gaussian prior. We use the following criteria to determine whether the estimated TTVs warrant further consideration in our full light-curve model: (1) more than three high-quality transits, (2) a TTV standard deviation greater than the photometric exposure time (i.e., 2 minutes), and (3) a single-transit S/N of 2 or greater. Since we expect a linear ephemeris for most planets in our sample, we do not offer an in-depth analysis of these variations here and

Table 3
Stellar Properties

TOI	m_K (mag)	π (mas)	T_{eff} (K)	[Fe/H] (dex)	$R_\star$ ($R_\odot$)	$M_\star$ ($M_\odot$)	$\rho_\star$ (g cm^{-3})	Age (Gyr)	SpecMatch
260	6.55	49.51	4050^{+35}_{-30}	$-0.21^{+0.06}_{-0.09}$	$0.55^{+0.01}_{-0.01}$	$0.55^{+0.01}_{-0.01}$	$4.7^{+0.14}_{-0.2}$	$15.9^{+2.8}_{-5.5}$	emp
266	8.45	9.8	5617^{+74}_{-73}	$0.01^{+0.06}_{-0.06}$	$0.96^{+0.02}_{-0.02}$	$0.94^{+0.03}_{-0.03}$	$1.48^{+0.11}_{-0.1}$	$6.0^{+2.4}_{-2.3}$	syn
329	9.68	3.49	5613^{+78}_{-73}	$0.2^{+0.06}_{-0.06}$	$1.53^{+0.03}_{-0.03}$	$1.07^{+0.03}_{-0.03}$	$0.41^{+0.03}_{-0.03}$	$8.7^{+1.0}_{-1.0}$	syn
465	9.34	8.16	4986^{+57}_{-56}	$0.3^{+0.06}_{-0.06}$	$0.83^{+0.01}_{-0.01}$	$0.87^{+0.02}_{-0.03}$	$2.15^{+0.15}_{-0.14}$	$5.6^{+3.9}_{-3.2}$	syn
469	7.59	14.64	5322^{+72}_{-70}	$0.33^{+0.06}_{-0.06}$	$0.98^{+0.02}_{-0.02}$	$0.95^{+0.03}_{-0.03}$	$1.39^{+0.1}_{-0.1}$	$8.6^{+2.8}_{-2.7}$	syn
480	6.01	18.31	6173^{+89}_{-118}	$0.16^{+0.06}_{-0.07}$	$1.49^{+0.04}_{-0.03}$	$1.28^{+0.03}_{-0.03}$	$0.54^{+0.04}_{-0.05}$	$2.7^{+0.6}_{-0.5}$	syn
509	6.88	20.39	5512^{+71}_{-72}	$0.11^{+0.05}_{-0.06}$	$0.96^{+0.02}_{-0.02}$	$0.94^{+0.03}_{-0.03}$	$1.49^{+0.1}_{-0.1}$	$6.6^{+2.5}_{-2.4}$	syn
554	5.71	21.89	6352^{+84}_{-76}	$-0.02^{+0.05}_{-0.06}$	$1.42^{+0.02}_{-0.02}$	$1.25^{+0.02}_{-0.02}$	$0.61^{+0.04}_{-0.03}$	$2.3^{+0.4}_{-0.4}$	syn
561	8.39	11.63	5342^{+57}_{-54}	$-0.3^{+0.06}_{-0.06}$	$0.86^{+0.01}_{-0.01}$	$0.76^{+0.02}_{-0.02}$	$1.69^{+0.11}_{-0.09}$	$16.1^{+2.4}_{-3.1}$	syn
669	9.13	6.97	5597^{+71}_{-72}	$0.0^{+0.06}_{-0.06}$	$0.99^{+0.02}_{-0.02}$	$0.92^{+0.03}_{-0.03}$	$1.34^{+0.1}_{-0.09}$	$7.9^{+2.3}_{-2.2}$	syn
1136	8.03	11.8	5805^{+57}_{-57}	$0.08^{+0.05}_{-0.05}$	$0.96^{+0.01}_{-0.01}$	$1.04^{+0.02}_{-0.02}$	$1.66^{+0.06}_{-0.07}$	$0.7^{+0.9}_{-0.4}$	syn
1173	9.13	7.53	5414^{+62}_{-65}	$0.19^{+0.06}_{-0.06}$	$0.94^{+0.02}_{-0.02}$	$0.95^{+0.03}_{-0.03}$	$1.61^{+0.11}_{-0.1}$	$5.9^{+2.4}_{-2.4}$	syn
1174	8.96	10.54	5157^{+59}_{-57}	$-0.0^{+0.06}_{-0.06}$	$0.78^{+0.03}_{-0.02}$	$0.84^{+0.02}_{-0.02}$	$2.44^{+0.18}_{-0.25}$	$2.7^{+3.6}_{-1.9}$	syn
1180	8.59	13.86	4803^{+53}_{-52}	$0.07^{+0.08}_{-0.09}$	$0.74^{+0.02}_{-0.02}$	$0.78^{+0.02}_{-0.03}$	$2.66^{+0.22}_{-0.28}$	$5.0^{+6.3}_{-3.6}$	emp
1181	9.22	3.27	6045^{+88}_{-84}	$0.39^{+0.05}_{-0.06}$	$1.93^{+0.04}_{-0.04}$	$1.46^{+0.02}_{-0.03}$	$0.28^{+0.02}_{-0.02}$	$2.4^{+0.3}_{-0.3}$	syn
1184	8.32	17.04	4616^{+47}_{-48}	$0.02^{+0.08}_{-0.09}$	$0.7^{+0.02}_{-0.02}$	$0.73^{+0.02}_{-0.03}$	$3.0^{+0.24}_{-0.27}$	$5.3^{+6.6}_{-3.9}$	emp
1194	9.34	6.65	5393^{+64}_{-62}	$0.35^{+0.06}_{-0.06}$	$0.96^{+0.02}_{-0.01}$	$0.98^{+0.03}_{-0.03}$	$1.55^{+0.1}_{-0.1}$	$4.9^{+2.3}_{-2.1}$	syn
1244	9.42	9.72	4721^{+55}_{-54}	$0.03^{+0.09}_{-0.09}$	$0.72^{+0.02}_{-0.02}$	$0.75^{+0.02}_{-0.03}$	$2.78^{+0.24}_{-0.27}$	$5.9^{+6.8}_{-4.2}$	emp
1246	9.91	5.87	5213^{+70}_{-67}	$0.17^{+0.06}_{-0.06}$	$0.86^{+0.02}_{-0.02}$	$0.89^{+0.03}_{-0.03}$	$1.92^{+0.16}_{-0.15}$	$6.3^{+3.6}_{-3.2}$	syn
1247	7.5	13.51	5697^{+75}_{-72}	$-0.12^{+0.06}_{-0.06}$	$1.07^{+0.02}_{-0.02}$	$0.91^{+0.03}_{-0.03}$	$1.03^{+0.07}_{-0.07}$	$9.8^{+2.0}_{-2.0}$	syn
1248	9.87	5.9	5205^{+56}_{-61}	$0.22^{+0.06}_{-0.06}$	$0.87^{+0.01}_{-0.01}$	$0.9^{+0.03}_{-0.03}$	$1.93^{+0.13}_{-0.12}$	$5.5^{+3.0}_{-2.7}$	syn
1249	9.13	7.14	5496^{+68}_{-66}	$0.3^{+0.06}_{-0.06}$	$0.98^{+0.02}_{-0.02}$	$1.01^{+0.03}_{-0.03}$	$1.5^{+0.11}_{-0.1}$	$4.0^{+2.3}_{-2.0}$	syn
1255	7.92	15.13	5216^{+52}_{-52}	$0.25^{+0.08}_{-0.05}$	$0.84^{+0.01}_{-0.01}$	$0.93^{+0.02}_{-0.02}$	$2.19^{+0.08}_{-0.09}$	$1.2^{+1.5}_{-0.8}$	syn
1269	9.89	5.78	5499^{+63}_{-60}	$-0.05^{+0.06}_{-0.06}$	$0.85^{+0.01}_{-0.01}$	$0.9^{+0.02}_{-0.03}$	$2.04^{+0.12}_{-0.12}$	$3.1^{+2.3}_{-1.8}$	syn
1272	9.7	7.24	5065^{+52}_{-50}	$0.18^{+0.06}_{-0.06}$	$0.79^{+0.01}_{-0.01}$	$0.88^{+0.01}_{-0.02}$	$2.46^{+0.08}_{-0.09}$	$1.1^{+1.6}_{-0.8}$	syn
1279	8.89	9.31	5457^{+66}_{-67}	$-0.08^{+0.06}_{-0.06}$	$0.84^{+0.01}_{-0.01}$	$0.88^{+0.03}_{-0.03}$	$2.05^{+0.13}_{-0.13}$	$4.2^{+2.5}_{-2.2}$	syn
1288	8.78	8.68	5388^{+68}_{-66}	$0.26^{+0.06}_{-0.06}$	$0.96^{+0.02}_{-0.02}$	$0.96^{+0.03}_{-0.03}$	$1.52^{+0.11}_{-0.1}$	$6.5^{+2.6}_{-2.5}$	syn
1294	9.96	2.98	5718^{+58}_{-77}	$0.28^{+0.06}_{-0.06}$	$1.56^{+0.03}_{-0.03}$	$1.16^{+0.06}_{-0.05}$	$0.43^{+0.03}_{-0.03}$	$6.2^{+1.4}_{-1.4}$	syn
1296	9.74	3.06	5567^{+77}_{-72}	$0.4^{+0.06}_{-0.02}$	$1.7^{+0.03}_{-0.03}$	$1.16^{+0.03}_{-0.02}$	$0.33^{+0.02}_{-0.02}$	$7.1^{+0.6}_{-0.7}$	syn
1298	10.01	3.11	5752^{+68}_{-98}	$0.4^{+0.06}_{-0.06}$	$1.45^{+0.03}_{-0.03}$	$1.22^{+0.02}_{-0.06}$	$0.55^{+0.03}_{-0.04}$	$4.3^{+1.7}_{-0.6}$	syn
1339	7.18	18.62	5385^{+69}_{-64}	$-0.14^{+0.06}_{-0.06}$	$0.93^{+0.02}_{-0.02}$	$0.82^{+0.03}_{-0.03}$	$1.41^{+0.1}_{-0.09}$	$13.9^{+2.8}_{-2.7}$	syn
1347	9.62	6.75	5493^{+53}_{-55}	$0.02^{+0.06}_{-0.05}$	$0.84^{+0.01}_{-0.01}$	$0.93^{+0.02}_{-0.02}$	$2.19^{+0.08}_{-0.08}$	$0.8^{+1.1}_{-0.6}$	syn
1386	9.09	6.78	5734^{+75}_{-76}	$0.15^{+0.06}_{-0.06}$	$1.02^{+0.02}_{-0.02}$	$1.04^{+0.03}_{-0.04}$	$1.35^{+0.09}_{-0.09}$	$3.2^{+1.9}_{-1.6}$	syn
1410	8.58	13.72	4635^{+52}_{-51}	$0.33^{+0.08}_{-0.09}$	$0.76^{+0.02}_{-0.02}$	$0.79^{+0.02}_{-0.02}$	$2.57^{+0.22}_{-0.28}$	$6.6^{+6.6}_{-4.6}$	emp
1411	7.25	30.76	4115^{+41}_{-45}	$0.01^{+0.07}_{-0.07}$	$0.61^{+0.02}_{-0.02}$	$0.6^{+0.01}_{-0.01}$	$3.63^{+0.23}_{-0.23}$	$9.6^{+6.6}_{-6.3}$	emp
1422	9.19	6.42	5810^{+81}_{-80}	$-0.03^{+0.06}_{-0.06}$	$1.02^{+0.02}_{-0.02}$	$0.99^{+0.04}_{-0.04}$	$1.29^{+0.09}_{-0.09}$	$4.6^{+2.0}_{-1.8}$	syn
1430	7.08	24.26	5086^{+62}_{-59}	$0.11^{+0.06}_{-0.06}$	$0.8^{+0.03}_{-0.02}$	$0.85^{+0.02}_{-0.02}$	$2.34^{+0.19}_{-0.26}$	$3.4^{+4.3}_{-2.4}$	syn
1436	9.72	7.57	5029^{+58}_{-57}	$-0.13^{+0.06}_{-0.06}$	$0.75^{+0.03}_{-0.02}$	$0.77^{+0.02}_{-0.03}$	$2.58^{+0.28}_{-0.32}$	$5.9^{+5.9}_{-4.0}$	syn
1437	7.82	9.65	5985^{+82}_{-81}	$-0.16^{+0.03}_{-0.05}$	$1.26^{+0.02}_{-0.02}$	$1.01^{+0.04}_{-0.04}$	$0.71^{+0.05}_{-0.05}$	$6.7^{+1.4}_{-1.3}$	syn
1438	9.09	9.02	5237^{+55}_{-55}	$0.08^{+0.05}_{-0.05}$	$0.82^{+0.01}_{-0.01}$	$0.89^{+0.02}_{-0.02}$	$2.29^{+0.1}_{-0.13}$	$2.2^{+2.2}_{-1.5}$	syn
1439	9.05	4.31	5840^{+63}_{-64}	$0.23^{+0.06}_{-0.07}$	$1.62^{+0.03}_{-0.03}$	$1.23^{+0.04}_{-0.08}$	$0.4^{+0.02}_{-0.03}$	$4.6^{+1.6}_{-0.7}$	syn
1443	8.67	11.63	5223^{+58}_{-57}	$-0.29^{+0.06}_{-0.06}$	$0.75^{+0.03}_{-0.03}$	$0.77^{+0.02}_{-0.02}$	$2.49^{+0.33}_{-0.35}$	$7.4^{+5.9}_{-4.8}$	syn
1444	9.06	7.94	5460^{+66}_{-66}	$0.15^{+0.06}_{-0.06}$	$0.91^{+0.02}_{-0.01}$	$0.95^{+0.03}_{-0.03}$	$1.76^{+0.12}_{-0.11}$	$3.8^{+2.5}_{-2.1}$	syn
1451	8.07	10.85	5800^{+77}_{-78}	$0.02^{+0.06}_{-0.06}$	$1.02^{+0.02}_{-0.02}$	$1.0^{+0.04}_{-0.03}$	$1.34^{+0.09}_{-0.09}$	$4.0^{+1.9}_{-1.7}$	syn
1456	7.24	12.37	6127^{+87}_{-79}	$0.04^{+0.06}_{-0.06}$	$1.27^{+0.02}_{-0.02}$	$1.16^{+0.03}_{-0.03}$	$0.8^{+0.05}_{-0.04}$	$2.9^{+0.9}_{-0.8}$	syn
1467	8.57	26.68	3775^{+22}_{-20}	$-0.06^{+0.04}_{-0.05}$	$0.46^{+0.01}_{-0.01}$	$0.45^{+0.01}_{-0.01}$	$6.65^{+0.22}_{-0.24}$	$13.4^{+4.4}_{-6.4}$	emp
1471	7.56	14.78	5648^{+74}_{-70}	$-0.02^{+0.06}_{-0.06}$	$0.96^{+0.02}_{-0.02}$	$0.94^{+0.03}_{-0.03}$	$1.49^{+0.11}_{-0.1}$	$5.6^{+2.3}_{-2.2}$	syn
1472	9.28	8.18	5132^{+54}_{-53}	$0.29^{+0.06}_{-0.06}$	$0.84^{+0.01}_{-0.01}$	$0.92^{+0.02}_{-0.02}$	$2.18^{+0.1}_{-0.13}$	$2.3^{+2.5}_{-1.5}$	syn
1473	7.39	14.76	5934^{+74}_{-78}	$-0.05^{+0.06}_{-0.05}$	$1.01^{+0.02}_{-0.02}$	$1.03^{+0.03}_{-0.04}$	$1.41^{+0.09}_{-0.09}$	$2.4^{+1.6}_{-1.3}$	syn
1601	9.19	2.94	5982^{+78}_{-64}	$0.34^{+0.05}_{-0.06}$	$2.2^{+0.06}_{-0.06}$	$1.51^{+0.03}_{-0.05}$	$0.2^{+0.02}_{-0.02}$	$2.4^{+0.4}_{-0.2}$	syn
1611	6.31	35.31	5106^{+66}_{-63}	$-0.03^{+0.06}_{-0.06}$	$0.78^{+0.03}_{-0.03}$	$0.82^{+0.02}_{-0.03}$	$2.38^{+0.25}_{-0.31}$	$4.7^{+5.1}_{-3.2}$	syn
1669	8.46	8.96	5497^{+73}_{-72}	$0.27^{+0.06}_{-0.06}$	$1.06^{+0.02}_{-0.02}$	$0.99^{+0.03}_{-0.03}$	$1.17^{+0.08}_{-0.08}$	$7.7^{+2.2}_{-2.1}$	syn
1691	8.54	8.94	5641^{+80}_{-74}	$0.05^{+0.06}_{-0.06}$	$1.01^{+0.02}_{-0.02}$	$0.96^{+0.04}_{-0.03}$	$1.3^{+0.1}_{-0.09}$	$6.6^{+2.3}_{-2.2}$	syn
1694	9.43	7.99	5058^{+60}_{-55}	$0.13^{+0.05}_{-0.06}$	$0.8^{+0.01}_{-0.01}$	$0.85^{+0.02}_{-0.02}$	$2.3^{+0.14}_{-0.15}$	$4.3^{+3.5}_{-2.6}$	syn
1710	7.96	12.28	5684^{+63}_{-67}	$0.15^{+0.04}_{-0.05}$	$0.96^{+0.02}_{-0.02}$	$1.03^{+0.02}_{-0.03}$	$1.64^{+0.08}_{-0.09}$	$1.5^{+1.6}_{-1.0}$	syn
1716	7.93	9.57	5877^{+78}_{-78}	$0.1^{+0.06}_{-0.06}$	$1.22^{+0.02}_{-0.02}$	$1.07^{+0.04}_{-0.04}$	$0.83^{+0.06}_{-0.06}$	$5.4^{+1.4}_{-1.3}$	syn
1723	8.13	9.9	5742^{+82}_{-80}	$0.16^{+0.05}_{-0.06}$	$1.09^{+0.02}_{-0.02}$	$1.04^{+0.04}_{-0.04}$	$1.13^{+0.09}_{-0.08}$	$4.8^{+1.9}_{-1.8}$	syn

Table 3
(Continued)

TOI	m_K (mag)	π (mas)	$T_{\rm eff}$ (K)	[Fe/H] (dex)	$R_\star$ ($R_\odot$)	$M_\star$ ($M_\odot$)	$\rho_\star$ (g cm^{-3})	Age (Gyr)	SpecMatch
1726	5.26	44.61	5634^{+62}_{-64}	$0.08^{+0.05}_{-0.05}$	$0.92^{+0.01}_{-0.01}$	$0.99^{+0.02}_{-0.03}$	$1.8^{+0.08}_{-0.09}$	$1.5^{+1.6}_{-1.0}$	syn
1736	7.28	11.21	5636^{+86}_{-79}	$0.15^{+0.06}_{-0.06}$	$1.43^{+0.03}_{-0.02}$	$1.04^{+0.04}_{-0.03}$	$0.5^{+0.04}_{-0.03}$	$9.2^{+1.3}_{-1.4}$	syn
1742	7.34	13.69	5814^{+75}_{-72}	$0.19^{+0.06}_{-0.06}$	$1.13^{+0.02}_{-0.02}$	$1.09^{+0.03}_{-0.03}$	$1.05^{+0.07}_{-0.06}$	$3.9^{+1.5}_{-1.3}$	syn
1751	7.93	8.79	5970^{+85}_{-83}	$-0.37^{+0.06}_{-0.06}$	$1.31^{+0.03}_{-0.02}$	$0.94^{+0.04}_{-0.03}$	$0.58^{+0.04}_{-0.04}$	$9.0^{+1.4}_{-1.4}$	syn
1753	10.18	4.38	5620^{+75}_{-71}	$0.03^{+0.06}_{-0.06}$	$0.97^{+0.02}_{-0.02}$	$0.95^{+0.03}_{-0.03}$	$1.44^{+0.12}_{-0.11}$	$5.9^{+2.4}_{-2.3}$	syn
1758	8.81	10.32	5150^{+64}_{-59}	$-0.02^{+0.06}_{-0.06}$	$0.82^{+0.01}_{-0.01}$	$0.83^{+0.03}_{-0.03}$	$2.13^{+0.15}_{-0.15}$	$7.5^{+3.7}_{-3.2}$	syn
1759	7.93	24.93	3930^{+32}_{-29}	$0.08^{+0.04}_{-0.04}$	$0.57^{+0.01}_{-0.01}$	$0.57^{+0.01}_{-0.01}$	$4.18^{+0.15}_{-0.17}$	$15.1^{+3.4}_{-5.4}$	emp
1775	9.72	6.67	5283^{+50}_{-51}	$0.16^{+0.03}_{-0.05}$	$0.83^{+0.01}_{-0.01}$	$0.92^{+0.01}_{-0.02}$	$2.27^{+0.07}_{-0.08}$	$0.8^{+1.1}_{-0.5}$	syn
1776	6.69	22.37	5784^{+74}_{-71}	$-0.19^{+0.06}_{-0.06}$	$0.94^{+0.02}_{-0.02}$	$0.92^{+0.03}_{-0.02}$	$1.57^{+0.11}_{-0.1}$	$5.1^{+2.2}_{-2.0}$	syn
1778	7.62	10.03	6007^{+83}_{-87}	$0.22^{+0.06}_{-0.06}$	$1.32^{+0.02}_{-0.01}$	$1.2^{+0.03}_{-0.03}$	$0.73^{+0.03}_{-0.05}$	$3.1^{+0.9}_{-0.7}$	syn
1794	8.69	6.39	5631^{+77}_{-73}	$0.03^{+0.05}_{-0.06}$	$1.32^{+0.02}_{-0.02}$	$0.97^{+0.03}_{-0.03}$	$0.59^{+0.04}_{-0.04}$	$10.8^{+1.5}_{-1.5}$	syn
1797	7.78	12.12	5907^{+65}_{-71}	$0.11^{+0.06}_{-0.06}$	$1.03^{+0.02}_{-0.02}$	$1.08^{+0.03}_{-0.03}$	$1.38^{+0.07}_{-0.08}$	$1.3^{+1.2}_{-0.8}$	syn
1798	9.24	8.81	5106^{+53}_{-55}	$0.07^{+0.06}_{-0.05}$	$0.79^{+0.01}_{-0.01}$	$0.85^{+0.02}_{-0.02}$	$2.42^{+0.1}_{-0.13}$	$2.6^{+2.6}_{-1.7}$	syn
1799	7.38	16.07	5697^{+74}_{-68}	$-0.06^{+0.06}_{-0.05}$	$0.95^{+0.02}_{-0.02}$	$0.94^{+0.03}_{-0.03}$	$1.52^{+0.1}_{-0.1}$	$5.1^{+2.2}_{-2.0}$	syn
1801	7.8	32.57	3747^{+24}_{-23}	$0.15^{+0.05}_{-0.04}$	$0.51^{+0.01}_{-0.01}$	$0.51^{+0.01}_{-0.01}$	$5.23^{+0.23}_{-0.23}$	$13.3^{+4.6}_{-6.6}$	emp
1807	7.57	23.46	4914^{+60}_{-57}	$0.04^{+0.09}_{-0.1}$	$0.75^{+0.02}_{-0.02}$	$0.8^{+0.02}_{-0.03}$	$2.72^{+0.18}_{-0.2}$	$2.1^{+3.4}_{-1.5}$	emp
1823	8.33	13.93	4926^{+57}_{-56}	$0.24^{+0.09}_{-0.09}$	$0.8^{+0.03}_{-0.03}$	$0.84^{+0.03}_{-0.03}$	$2.24^{+0.25}_{-0.31}$	$6.3^{+6.3}_{-4.4}$	emp
1824	7.76	16.8	5165^{+56}_{-56}	$0.12^{+0.06}_{-0.06}$	$0.81^{+0.01}_{-0.01}$	$0.88^{+0.02}_{-0.02}$	$2.3^{+0.1}_{-0.13}$	$2.5^{+2.5}_{-1.6}$	syn
1836	8.53	5.19	6237^{+91}_{-68}	$-0.14^{+0.07}_{-0.03}$	$1.65^{+0.03}_{-0.03}$	$1.25^{+0.02}_{-0.04}$	$0.39^{+0.02}_{-0.02}$	$3.2^{+0.7}_{-0.3}$	syn
1842	8.45	4.45	6039^{+93}_{-88}	$0.33^{+0.06}_{-0.06}$	$2.03^{+0.04}_{-0.04}$	$1.46^{+0.03}_{-0.04}$	$0.24^{+0.02}_{-0.02}$	$2.5^{+0.4}_{-0.3}$	syn
1898	6.66	12.52	6241^{+88}_{-84}	$-0.1^{+0.06}_{-0.07}$	$1.61^{+0.03}_{-0.03}$	$1.25^{+0.03}_{-0.04}$	$0.41^{+0.03}_{-0.02}$	$3.1^{+0.6}_{-0.5}$	syn
2019	8.6	5.02	5625^{+77}_{-77}	$0.41^{+0.06}_{-0.06}$	$1.75^{+0.03}_{-0.03}$	$1.18^{+0.11}_{-0.02}$	$0.31^{+0.03}_{-0.02}$	$6.4^{+0.6}_{-1.9}$	syn
2045	9.85	2.7	6045^{+75}_{-68}	$0.07^{+0.06}_{-0.04}$	$1.78^{+0.04}_{-0.04}$	$1.29^{+0.03}_{-0.08}$	$0.32^{+0.02}_{-0.02}$	$3.4^{+1.2}_{-0.4}$	syn
2076	7.12	23.83	5191^{+61}_{-57}	$0.02^{+0.06}_{-0.06}$	$0.8^{+0.03}_{-0.02}$	$0.86^{+0.02}_{-0.02}$	$2.36^{+0.19}_{-0.25}$	$2.7^{+3.6}_{-1.9}$	syn
2088	9.52	7.88	5080^{+55}_{-54}	$0.34^{+0.06}_{-0.06}$	$0.85^{+0.03}_{-0.03}$	$0.9^{+0.02}_{-0.03}$	$2.05^{+0.2}_{-0.26}$	$4.5^{+4.6}_{-3.1}$	syn
2114	9.09	3.12	6359^{+88}_{-85}	$0.11^{+0.05}_{-0.06}$	$2.1^{+0.04}_{-0.04}$	$1.48^{+0.03}_{-0.04}$	$0.23^{+0.01}_{-0.01}$	$2.0^{+0.2}_{-0.2}$	syn
2128	5.82	27.31	5967^{+85}_{-84}	$-0.07^{+0.05}_{-0.06}$	$1.12^{+0.02}_{-0.02}$	$1.03^{+0.04}_{-0.04}$	$1.02^{+0.08}_{-0.08}$	$4.7^{+1.7}_{-1.5}$	syn
2145	7.76	4.42	6200^{+83}_{-81}	$0.29^{+0.06}_{-0.05}$	$2.75^{+0.06}_{-0.05}$	$1.72^{+0.03}_{-0.04}$	$0.11^{+0.01}_{-0.01}$	$1.6^{+0.2}_{-0.1}$	syn

Note. Properties of 85 planet hosting stars from the TKS sample (Chontos et al. 2022). m_K is 2MASS K-band apparent magnitude, and π is Gaia DR2 parallax. $T_{\rm eff}$, [Fe/H], $R_\star$, $M_\star$, $\rho_\star$, and age were derived using `isoclassify` isochrone modeling (Huber et al. 2017) as described in Section 2.2. The given values reflect median measurements with upper and lower uncertainties. The last column denotes which `SpecMatch` method was used to derive the initial stellar property inputs to `isoclassify`: "syn"—SpecMatch-Synthetic or "emp"—SpecMatch-Empirical (see Section 2.1).

(This table is available in machine-readable form.)

instead leave that analysis to later work (see Section 5.3 for more details).

3.5. Full Light-curve Model

We use the MAP values of all model parameters from both our trend model and TTV model as well-informed initial guesses for a complete MAP fit to the normalized light-curve photometry. We simultaneously fit for the stellar variability trend, transit times, and transit shape using `exoplanet` with the same model priors as were used in our previous MAP fits. This full model allows us to measure photometric variability via GPs (as was done in Section 3.3) while also accounting for the true transit shapes and times. We subtract this MAP fit of the photometric variability to produce the final detrended light curve for our analysis (see Figure 4 for an example). We create a transit mask using the MAP values from this full model fit to exclude out-of-transit photometry beyond ± 2.5 $T_{14,\rm MAP}$ from each transit midpoint time, removing data that are uninformative of the transit fit in order to improve posterior sampling efficiency.

With our fully detrended photometry and TTV estimates from this full MAP fit, we build our final model intended for

posterior sampling and robustly fitting the transit shape. For planets with TTV estimates below the thresholds described in Section 3.4, we assume a linear ephemeris and do not directly fit transit times in the final model. Altogether, we fit for $\{P, t_0, R_p/R_\star, b, T_{14}, u_1, u_2, \mu, \sigma_{\rm LC}\}$ and sometimes transit times $\{TT_i\}$, conditioned on our fully detrended TESS light curve.

We apply priors to each of the light-curve model parameters, briefly outlined below and in Table 2. We apply Gaussian priors on t_0, μ, u_1, and u_2, each centered on estimates that were reasonably well constrained from earlier analysis. We use a lognormal prior on $\sigma_{\rm LC}$ to ensure positive values, with $\mu(\sigma_{\rm LC}) = \log(\sigma_{\rm flux})$ and $\sigma(\sigma_{\rm LC}) = 1$. For $R_p/R_\star$ and T_{14}, we use log-uniform priors with upper and lower bounds described in Table 2, designed to minimize the effect that these boundaries have on the completeness of the posterior sampling. We also model b with a uniform prior from 0 to $1 + R_p/R_\star$ to encompass the regime of grazing transits in our posterior space.

Here we use T_{14} to directly fit the transit duration rather than measuring it through indirect means such as sampling in "circular" stellar density (see, e.g., Dawson & Johnson 2012) or simultaneously fitting the true stellar density ($\rho_\star$), eccentricity (e), and argument of periastron (ω). While the former

Table 4
Planet Properties

Planet	P (days)	t_0 BTJD	$R_p/R_\star$ %	R_p ($R_\oplus$)	T_{14} (hr)	T_{circ} (hr)	a (au)	TTVs? y/n
260.01	$13.475832^{+4.5e-05}_{-5.6e-05}$	$1392.2944^{+0.0021}_{-0.0023}$	$2.47^{+0.2}_{-0.14}$	$1.47^{+0.12}_{-0.08}$	$2.0^{+0.14}_{-0.13}$	$2.96^{+0.03}_{-0.04}$	$0.0907^{+0.0005}_{-0.0003}$	n
266.01	$10.751013^{+7.2e-05}_{-7e-05}$	$1393.0862^{+0.0035}_{-0.0032}$	$2.42^{+0.1}_{-0.12}$	$2.54^{+0.16}_{-0.14}$	$3.0^{+0.16}_{-0.13}$	$4.04^{+0.1}_{-0.09}$	$0.0933^{+0.0012}_{-0.0011}$	n
266.02	$19.605464^{+0.000228}_{-0.000237}$	$1398.2927^{+0.0087}_{-0.0059}$	$2.41^{+0.14}_{-0.13}$	$2.52^{+0.15}_{-0.14}$	$4.38^{+0.27}_{-0.21}$	$4.94^{+0.12}_{-0.11}$	$0.1393^{+0.0017}_{-0.0016}$	n
329.01	$5.70442^{+0.000116}_{-0.000101}$	$2090.7934^{+0.0043}_{-0.0057}$	$2.96^{+0.16}_{-0.14}$	$4.94^{+0.29}_{-0.26}$	$4.21^{+0.21}_{-0.18}$	$5.04^{+0.13}_{-0.11}$	$0.0639^{+0.0006}_{-0.0006}$	n
465.01	$3.836162^{+2e-06}_{-2e-06}$	$1414.1361^{+0.0004}_{-0.0003}$	$6.68^{+0.09}_{-0.07}$	$6.03^{+0.13}_{-0.12}$	$2.4^{+0.02}_{-0.02}$	$2.64^{+0.06}_{-0.05}$	$0.0458^{+0.0004}_{-0.0005}$	n
469.01	$13.630829^{+2.6e-05}_{-2.6e-05}$	$1474.5691^{+0.0011}_{-0.0011}$	$3.19^{+0.07}_{-0.06}$	$3.43^{+0.1}_{-0.09}$	$4.33^{+0.05}_{-0.04}$	$4.5^{+0.11}_{-0.11}$	$0.1096^{+0.0013}_{-0.0012}$	n
480.01	$6.865906^{+1.7e-05}_{-1.9e-05}$	$1469.5655^{+0.0016}_{-0.0015}$	$1.76^{+0.06}_{-0.05}$	$2.85^{+0.13}_{-0.1}$	$3.57^{+0.06}_{-0.06}$	$4.84^{+0.13}_{-0.15}$	$0.0767^{+0.0006}_{-0.0006}$	n
509.01	$9.058805^{+1.8e-05}_{-1.6e-05}$	$1494.4467^{+0.001}_{-0.001}$	$2.79^{+0.07}_{-0.06}$	$2.92^{+0.09}_{-0.08}$	$3.7^{+0.04}_{-0.04}$	$3.82^{+0.09}_{-0.09}$	$0.0833^{+0.001}_{-0.0009}$	n
509.02	$21.402464^{+0.001794}_{-0.001919}$	$1504.1438^{+0.067}_{-0.0622}$	$2.93^{+0.07}_{-0.06}$	$3.06^{+0.09}_{-0.08}$	$5.42^{+0.08}_{-0.08}$	$5.1^{+0.12}_{-0.12}$	$0.1478^{+0.0018}_{-0.0017}$	n
554.01	$3.04405^{+9e-06}_{-8e-06}$	$1438.4733^{+0.002}_{-0.0025}$	$0.88^{+0.08}_{-0.06}$	$1.36^{+0.13}_{-0.1}$	$1.35^{+0.06}_{-0.06}$	$3.52^{+0.08}_{-0.05}$	$0.0443^{+0.0003}_{-0.0003}$	n
554.02	$7.049157^{+1.3e-05}_{-1.4e-05}$	$1442.6179^{+0.0016}_{-0.0016}$	$1.65^{+0.07}_{-0.05}$	$2.55^{+0.11}_{-0.08}$	$3.35^{+0.06}_{-0.04}$	$4.68^{+0.1}_{-0.07}$	$0.0775^{+0.0005}_{-0.0005}$	n
561.01	$0.4465691^{+4e-07}_{-4e-07}$	$1517.9451^{+0.0007}_{-0.0008}$	$1.56^{+0.05}_{-0.04}$	$1.46^{+0.05}_{-0.05}$	$1.35^{+0.02}_{-0.02}$	$1.36^{+0.03}_{-0.03}$	$0.0104^{+0.0001}_{-0.0001}$	n
561.02	$10.778858^{+3.3e-05}_{-3.5e-05}$	$1527.0608^{+0.0025}_{-0.0023}$	$3.13^{+0.21}_{-0.09}$	$2.93^{+0.2}_{-0.1}$	$3.83^{+0.16}_{-0.1}$	$3.89^{+0.08}_{-0.07}$	$0.0872^{+0.0009}_{-0.0007}$	n
561.03	$25.712443^{+0.000111}_{-0.000122}$	$1521.8835^{+0.0038}_{-0.0036}$	$2.91^{+0.11}_{-0.09}$	$2.72^{+0.11}_{-0.1}$	$5.19^{+0.17}_{-0.12}$	$5.19^{+0.11}_{-0.09}$	$0.1556^{+0.0017}_{-0.0013}$	n
669.01	$3.945154^{+1.3e-05}_{-1.1e-05}$	$1546.1417^{+0.0021}_{-0.003}$	$2.4^{+0.1}_{-0.09}$	$2.59^{+0.13}_{-0.13}$	$2.87^{+0.1}_{-0.09}$	$2.99^{+0.07}_{-0.07}$	$0.0476^{+0.0006}_{-0.0005}$	n
1136.01	$6.258767^{+1.5e-05}_{-1.4e-05}$	$1688.7067^{+0.0013}_{-0.0012}$	$2.65^{+0.06}_{-0.05}$	$2.77^{+0.08}_{-0.07}$	$3.49^{+0.05}_{-0.04}$	$3.25^{+0.04}_{-0.04}$	$0.0673^{+0.0004}_{-0.0004}$	y
1136.02	$12.518595^{+1.5e-05}_{-1.5e-05}$	$1686.0634^{+0.0005}_{-0.0006}$	$4.43^{+0.13}_{-0.08}$	$4.62^{+0.15}_{-0.1}$	$4.13^{+0.07}_{-0.06}$	$4.17^{+0.05}_{-0.06}$	$0.1069^{+0.0006}_{-0.0007}$	y
1136.03	$18.797505^{+0.000141}_{-0.000121}$	$1697.799^{+0.004}_{-0.0045}$	$2.44^{+0.09}_{-0.08}$	$2.55^{+0.1}_{-0.09}$	$4.46^{+0.11}_{-0.09}$	$4.68^{+0.06}_{-0.06}$	$0.1402^{+0.0008}_{-0.0009}$	y
1136.04	$26.317767^{+4.7e-05}_{-4.7e-05}$	$1699.3798^{+0.0011}_{-0.0011}$	$3.58^{+0.06}_{-0.06}$	$3.74^{+0.09}_{-0.08}$	$5.18^{+0.05}_{-0.05}$	$5.3^{+0.07}_{-0.07}$	$0.1755^{+0.001}_{-0.0011}$	y
1173.01	$7.064397^{+3e-06}_{-3e-06}$	$1688.7154^{+0.0002}_{-0.0002}$	$8.83^{+0.06}_{-0.06}$	$9.02^{+0.16}_{-0.15}$	$2.56^{+0.02}_{-0.02}$	$3.63^{+0.08}_{-0.08}$	$0.0707^{+0.0008}_{-0.0007}$	n
1174.01	$8.9534^{+4.1e-05}_{-3.9e-05}$	$1690.0626^{+0.0022}_{-0.0026}$	$2.93^{+0.13}_{-0.1}$	$2.51^{+0.14}_{-0.11}$	$3.0^{+0.12}_{-0.1}$	$3.23^{+0.08}_{-0.11}$	$0.0797^{+0.0006}_{-0.0007}$	n
1180.01	$9.686755^{+1.2e-05}_{-1.2e-05}$	$1691.0488^{+0.0009}_{-0.0009}$	$3.75^{+0.2}_{-0.12}$	$3.04^{+0.19}_{-0.13}$	$2.76^{+0.08}_{-0.06}$	$3.25^{+0.09}_{-0.11}$	$0.0818^{+0.0008}_{-0.0009}$	n
1181.01	$2.1031937^{+3e-07}_{-3e-07}$	$1957.8213^{+0.0001}_{-0.0001}$	$7.68^{+0.02}_{-0.02}$	$16.2^{+0.33}_{-0.34}$	$4.12^{+0.01}_{-0.01}$	$4.33^{+0.09}_{-0.08}$	$0.0364^{+0.0002}_{-0.0002}$	n
1184.01	$5.748431^{+3e-06}_{-3e-06}$	$1684.3594^{+0.0005}_{-0.0005}$	$3.17^{+0.09}_{-0.16}$	$2.41^{+0.1}_{-0.14}$	$1.88^{+0.03}_{-0.03}$	$2.61^{+0.07}_{-0.08}$	$0.0565^{+0.0006}_{-0.0006}$	n
1194.01	$2.310645^{+1e-06}_{-1e-06}$	$1684.9235^{+0.0002}_{-0.0002}$	$8.32^{+0.06}_{-0.06}$	$8.72^{+0.16}_{-0.15}$	$1.63^{+0.01}_{-0.01}$	$2.53^{+0.06}_{-0.05}$	$0.034^{+0.0003}_{-0.0003}$	n
1244.01	$6.400317^{+8e-06}_{-8e-06}$	$1684.9474^{+0.0008}_{-0.0008}$	$3.01^{+0.14}_{-0.1}$	$2.38^{+0.13}_{-0.11}$	$2.22^{+0.04}_{-0.04}$	$2.77^{+0.08}_{-0.09}$	$0.0614^{+0.0007}_{-0.0007}$	n
1246.01	$4.30744^{+4e-06}_{-3e-06}$	$1686.5661^{+0.0007}_{-0.0008}$	$3.05^{+0.12}_{-0.08}$	$2.87^{+0.13}_{-0.1}$	$2.18^{+0.04}_{-0.03}$	$2.75^{+0.08}_{-0.07}$	$0.0498^{+0.0006}_{-0.0006}$	n
1246.02	$5.904141^{+1.3e-05}_{-1.4e-05}$	$1683.4664^{+0.0016}_{-0.0016}$	$2.6^{+0.14}_{-0.08}$	$2.45^{+0.14}_{-0.09}$	$2.89^{+0.07}_{-0.07}$	$3.04^{+0.08}_{-0.08}$	$0.0615^{+0.0007}_{-0.0007}$	n
1246.03	$18.654958^{+4.9e-05}_{-4.7e-05}$	$1688.9746^{+0.002}_{-0.002}$	$3.64^{+0.14}_{-0.1}$	$3.43^{+0.15}_{-0.12}$	$3.95^{+0.1}_{-0.08}$	$4.5^{+0.12}_{-0.12}$	$0.1324^{+0.0015}_{-0.0015}$	y
1246.04	$37.925389^{+0.000149}_{-0.000156}$	$1700.6956^{+0.0033}_{-0.0034}$	$3.73^{+0.27}_{-0.18}$	$3.51^{+0.27}_{-0.18}$	$3.54^{+0.16}_{-0.12}$	$5.71^{+0.16}_{-0.15}$	$0.2124^{+0.0024}_{-0.0024}$	y
1247.01	$15.923365^{+3.4e-05}_{-3.6e-05}$	$1687.6494^{+0.0014}_{-0.0014}$	$2.16^{+0.06}_{-0.05}$	$2.53^{+0.08}_{-0.07}$	$4.33^{+0.07}_{-0.07}$	$5.18^{+0.12}_{-0.11}$	$0.1202^{+0.0014}_{-0.0013}$	n
1248.01	$4.360156^{+1e-06}_{-1e-06}$	$1687.1212^{+0.0002}_{-0.0002}$	$7.19^{+0.05}_{-0.06}$	$6.81^{+0.12}_{-0.12}$	$2.31^{+0.01}_{-0.01}$	$2.87^{+0.06}_{-0.06}$	$0.0505^{+0.0005}_{-0.0005}$	n
1249.01	$13.079163^{+6.3e-05}_{-6.3e-05}$	$1694.3786^{+0.0027}_{-0.0029}$	$3.06^{+0.28}_{-0.17}$	$3.27^{+0.31}_{-0.19}$	$3.15^{+0.26}_{-0.15}$	$4.32^{+0.1}_{-0.1}$	$0.1089^{+0.0011}_{-0.0011}$	n
1255.01	$10.288889^{+4e-06}_{-4e-06}$	$1691.6544^{+0.0004}_{-0.0003}$	$2.7^{+0.07}_{-0.05}$	$2.48^{+0.07}_{-0.05}$	$1.53^{+0.02}_{-0.01}$	$3.5^{+0.04}_{-0.05}$	$0.0905^{+0.0005}_{-0.0005}$	n
1269.01	$4.252989^{+6e-06}_{-6e-06}$	$1686.6058^{+0.0009}_{-0.0013}$	$2.58^{+0.16}_{-0.07}$	$2.4^{+0.15}_{-0.07}$	$2.62^{+0.07}_{-0.05}$	$2.67^{+0.05}_{-0.05}$	$0.0496^{+0.0005}_{-0.0005}$	n
1269.02	$9.237875^{+2e-05}_{-2e-05}$	$1685.9772^{+0.0022}_{-0.0017}$	$2.45^{+0.12}_{-0.09}$	$2.27^{+0.12}_{-0.09}$	$2.72^{+0.07}_{-0.07}$	$3.45^{+0.07}_{-0.07}$	$0.0833^{+0.0008}_{-0.0008}$	n
1272.01	$3.315979^{+6e-06}_{-5e-06}$	$1713.0315^{+0.0006}_{-0.0006}$	$4.77^{+0.25}_{-0.17}$	$4.13^{+0.23}_{-0.15}$	$1.57^{+0.06}_{-0.05}$	$2.36^{+0.03}_{-0.03}$	$0.0417^{+0.0002}_{-0.0003}$	n
1279.01	$9.614216^{+3.7e-05}_{-3.5e-05}$	$1717.4777^{+0.0026}_{-0.0027}$	$2.9^{+0.14}_{-0.11}$	$2.66^{+0.14}_{-0.11}$	$2.76^{+0.11}_{-0.09}$	$3.5^{+0.07}_{-0.07}$	$0.0847^{+0.0009}_{-0.0008}$	y
1288.01	$2.699831^{+1e-06}_{-1e-06}$	$1712.3587^{+0.0002}_{-0.0002}$	$4.75^{+0.06}_{-0.05}$	$4.97^{+0.11}_{-0.1}$	$2.38^{+0.01}_{-0.01}$	$2.59^{+0.06}_{-0.06}$	$0.0374^{+0.0004}_{-0.0004}$	n
1294.01	$3.915289^{+1.6e-05}_{-1.6e-05}$	$2393.0074^{+0.0007}_{-0.0007}$	$5.96^{+0.08}_{-0.08}$	$10.12^{+0.24}_{-0.22}$	$3.03^{+0.05}_{-0.05}$	$4.51^{+0.1}_{-0.12}$	$0.051^{+0.0009}_{-0.0007}$	n
1296.01	$3.944373^{+1e-06}_{-1e-06}$	$1930.7553^{+0.0002}_{-0.0002}$	$7.6^{+0.04}_{-0.04}$	$14.12^{+0.28}_{-0.26}$	$4.86^{+0.01}_{-0.01}$	$5.04^{+0.12}_{-0.1}$	$0.0513^{+0.0004}_{-0.0003}$	n
1298.01	$4.537142^{+2e-06}_{-2e-06}$	$1934.1225^{+0.0003}_{-0.0003}$	$6.09^{+0.05}_{-0.04}$	$9.66^{+0.2}_{-0.17}$	$4.03^{+0.02}_{-0.02}$	$4.38^{+0.09}_{-0.1}$	$0.0573^{+0.0004}_{-0.0009}$	n
1339.01	$8.880322^{+3e-06}_{-3e-06}$	$1715.3558^{+0.0003}_{-0.0002}$	$3.33^{+0.05}_{-0.07}$	$3.4^{+0.08}_{-0.09}$	$3.07^{+0.02}_{-0.02}$	$3.89^{+0.09}_{-0.08}$	$0.0786^{+0.0009}_{-0.0008}$	n
1339.02	$28.579984^{+2.4e-05}_{-2.4e-05}$	$1726.0547^{+0.0006}_{-0.0006}$	$3.12^{+0.08}_{-0.07}$	$3.18^{+0.1}_{-0.09}$	$4.47^{+0.05}_{-0.04}$	$5.73^{+0.14}_{-0.12}$	$0.1714^{+0.0019}_{-0.0018}$	y
1339.03	$38.352218^{+4.2e-05}_{-4.1e-05}$	$1743.556^{+0.0008}_{-0.0007}$	$3.06^{+0.05}_{-0.05}$	$3.12^{+0.07}_{-0.07}$	$5.51^{+0.05}_{-0.05}$	$6.31^{+0.15}_{-0.13}$	$0.2085^{+0.0023}_{-0.0022}$	y
1347.01	$0.8474247^{+4e-07}_{-4e-07}$	$1683.5587^{+0.0003}_{-0.0003}$	$1.98^{+0.09}_{-0.06}$	$1.81^{+0.09}_{-0.06}$	$0.88^{+0.02}_{-0.01}$	$1.53^{+0.02}_{-0.02}$	$0.0171^{+0.0001}_{-0.0001}$	n
1347.02	$4.84195^{+1.3e-05}_{-1.2e-05}$	$1688.1903^{+0.0017}_{-0.002}$	$1.83^{+0.09}_{-0.07}$	$1.68^{+0.09}_{-0.07}$	$2.24^{+0.09}_{-0.08}$	$2.7^{+0.03}_{-0.03}$	$0.0546^{+0.0003}_{-0.0003}$	n
1386.01	$25.840653^{+0.003119}_{-0.003192}$	$1752.3213^{+0.0022}_{-0.002}$	$5.57^{+0.16}_{-0.12}$	$6.22^{+0.21}_{-0.12}$	$5.67^{+0.15}_{-0.13}$	$5.75^{+0.13}_{-0.13}$	$0.1731^{+0.0019}_{-0.002}$	n
1410.01	$1.216876^{+1e-06}_{-1e-06}$	$1739.7293^{+0.0006}_{-0.0006}$	$3.76^{+0.24}_{-0.17}$	$3.1^{+0.22}_{-0.16}$	$1.11^{+0.05}_{-0.04}$	$1.66^{+0.05}_{-0.06}$	$0.0207^{+0.0002}_{-0.0002}$	n
1411.01	$1.452053^{+2e-06}_{-2e-06}$	$1739.474^{+0.0005}_{-0.0005}$	$1.79^{+0.05}_{-0.04}$	$1.2^{+0.05}_{-0.04}$	$1.51^{+0.02}_{-0.02}$	$1.53^{+0.03}_{-0.03}$	$0.0212^{+0.0002}_{-0.0002}$	n
1422.01	$13.001782^{+5e-05}_{-4.2e-05}$	$1745.9141^{+0.0018}_{-0.0016}$	$3.53^{+0.12}_{-0.09}$	$3.94^{+0.15}_{-0.13}$	$4.44^{+0.11}_{-0.09}$	$4.55^{+0.11}_{-0.11}$	$0.1079^{+0.0013}_{-0.0013}$	n
1430.01	$7.434098^{+9e-06}_{-9e-06}$	$1690.779^{+0.0009}_{-0.0009}$	$2.38^{+0.07}_{-0.05}$	$2.08^{+0.09}_{-0.07}$	$2.67^{+0.04}_{-0.04}$	$3.06^{+0.08}_{-0.11}$	$0.0707^{+0.0006}_{-0.0006}$	n
1436.01	$0.867617^{+2e-06}_{-3e-06}$	$1711.8961^{+0.0012}_{-0.0011}$	$1.87^{+0.1}_{-0.09}$	$1.52^{+0.1}_{-0.09}$	$1.32^{+0.05}_{-0.05}$	$1.45^{+0.05}_{-0.06}$	$0.0164^{+0.0002}_{-0.0002}$	n
1437.01	$18.840952^{+7.7e-05}_{-7.7e-05}$	$1700.7335^{+0.0029}_{-0.003}$	$1.77^{+0.04}_{-0.03}$	$2.43^{+0.07}_{-0.06}$	$6.19^{+0.12}_{-0.1}$	$6.19^{+0.15}_{-0.14}$	$0.1391^{+0.0017}_{-0.0017}$	n
1438.01	$5.139659^{+5e-06}_{-5e-06}$	$1683.6266^{+0.0007}_{-0.0007}$	$3.22^{+0.2}_{-0.34}$	$2.87^{+0.18}_{-0.3}$	$1.01^{+0.06}_{-0.1}$	$2.75^{+0.04}_{-0.05}$	$0.056^{+0.0004}_{-0.0004}$	n
1438.02	$9.428074^{+1.6e-05}_{-1.5e-05}$	$1689.9152^{+0.0014}_{-0.0014}$	$2.92^{+0.17}_{-0.3}$	$2.6^{+0.15}_{-0.27}$	$1.56^{+0.11}_{-0.1}$	$3.36^{+0.05}_{-0.06}$	$0.0839^{+0.0006}_{-0.0007}$	n
1439.01	$27.643869^{+0.000133}_{-0.000138}$	$1703.4782^{+0.004}_{-0.0039}$	$2.4^{+0.12}_{-0.09}$	$4.24^{+0.23}_{-0.17}$	$5.63^{+0.21}_{-0.14}$	$8.52^{+0.17}_{-0.2}$	$0.1918^{+0.0018}_{-0.004}$	n
1443.01	$23.540714^{+6.6e-05}_{-6.2e-05}$	$1693.2443^{+0.0023}_{-0.0025}$	$2.81^{+0.09}_{-0.07}$	$2.3^{+0.13}_{-0.1}$	$4.26^{+0.08}_{-0.07}$	$4.43^{+0.2}_{-0.21}$	$0.1471^{+0.0015}_{-0.0017}$	n

Table 4
(Continued)

Planet	P (days)	t_0 BTJD	$R_p/R_\star$ %	R_p ($R_\oplus$)	T_{14} (hr)	T_{circ} (hr)	a (au)	TTVs? y/n
1444.01	$0.4702737^{+3e-07}_{-3e-07}$	$1711.3666^{+0.0005}_{-0.0008}$	$1.43^{+0.04}_{-0.03}$	$1.42^{+0.05}_{-0.04}$	$1.28^{+0.02}_{-0.02}$	$1.36^{+0.03}_{-0.03}$	$0.0116^{+0.0001}_{-0.0001}$	n
1451.01	$16.537903^{+6.9e-05}_{-6.3e-05}$	$1694.3138^{+0.0021}_{-0.0029}$	$2.36^{+0.11}_{-0.08}$	$2.61^{+0.13}_{-0.1}$	$3.09^{+0.09}_{-0.07}$	$4.82^{+0.11}_{-0.11}$	$0.1271^{+0.0015}_{-0.0014}$	n
1456.01	$18.711796^{+1.4e-05}_{-1.4e-05}$	$1692.2609^{+0.0005}_{-0.0005}$	$6.57^{+0.06}_{-0.05}$	$9.07^{+0.19}_{-0.18}$	$6.17^{+0.03}_{-0.03}$	$6.21^{+0.14}_{-0.12}$	$0.1451^{+0.0013}_{-0.0014}$	y
1467.01	$5.971148^{+1.1e-05}_{-1e-05}$	$1766.9883^{+0.0013}_{-0.0022}$	$3.37^{+0.17}_{-0.16}$	$1.68^{+0.09}_{-0.08}$	$1.58^{+0.07}_{-0.05}$	$2.03^{+0.02}_{-0.02}$	$0.0494^{+0.0003}_{-0.0003}$	n
1471.01	$20.772891^{+4.8e-05}_{-5e-05}$	$1767.422^{+0.0014}_{-0.0014}$	$3.66^{+0.07}_{-0.06}$	$3.83^{+0.1}_{-0.09}$	$4.94^{+0.06}_{-0.05}$	$5.08^{+0.12}_{-0.11}$	$0.145^{+0.0017}_{-0.0017}$	n
1471.02	$52.563553^{+0.000166}_{-0.000185}$	$1779.1909^{+0.0016}_{-0.0014}$	$3.28^{+0.07}_{-0.06}$	$3.43^{+0.1}_{-0.09}$	$6.57^{+0.08}_{-0.08}$	$6.9^{+0.17}_{-0.15}$	$0.2692^{+0.0032}_{-0.0031}$	n
1472.01	$6.363386^{+9e-06}_{-8e-06}$	$1765.6096^{+0.0012}_{-0.0013}$	$4.55^{+0.15}_{-0.12}$	$4.16^{+0.16}_{-0.13}$	$2.61^{+0.06}_{-0.05}$	$3.04^{+0.05}_{-0.06}$	$0.0653^{+0.0005}_{-0.0005}$	n
1473.01	$5.254479^{+1.2e-05}_{-1.3e-05}$	$1769.7834^{+0.0026}_{-0.0019}$	$2.21^{+0.08}_{-0.06}$	$2.43^{+0.1}_{-0.07}$	$3.24^{+0.1}_{-0.07}$	$3.23^{+0.07}_{-0.07}$	$0.0597^{+0.0006}_{-0.0007}$	n
1601.01	$5.333298^{+0.000889}_{-0.000968}$	$1793.2752^{+0.0017}_{-0.0013}$	$5.93^{+0.21}_{-0.13}$	$14.2^{+0.65}_{-0.51}$	$6.49^{+0.13}_{-0.11}$	$6.5^{+0.18}_{-0.11}$	$0.0685^{+0.0005}_{-0.0008}$	n
1611.01	$16.201708^{+1.3e-05}_{-1.2e-05}$	$1796.495^{+0.0006}_{-0.0006}$	$2.74^{+0.09}_{-0.05}$	$2.34^{+0.12}_{-0.09}$	$2.9^{+0.03}_{-0.03}$	$3.96^{+0.14}_{-0.17}$	$0.1173^{+0.0011}_{-0.0012}$	y
1669.01	$2.680055^{+3e-06}_{-3e-06}$	$1816.9447^{+0.0009}_{-0.0009}$	$1.99^{+0.08}_{-0.07}$	$2.3^{+0.1}_{-0.09}$	$1.93^{+0.04}_{-0.03}$	$2.75^{+0.07}_{-0.06}$	$0.0376^{+0.0004}_{-0.0004}$	n
1691.01	$16.7369^{+3.2e-05}_{-3e-05}$	$1818.0907^{+0.0013}_{-0.0014}$	$3.24^{+0.08}_{-0.05}$	$3.57^{+0.11}_{-0.09}$	$4.97^{+0.07}_{-0.05}$	$4.92^{+0.12}_{-0.12}$	$0.1262^{+0.0016}_{-0.0015}$	n
1694.01	$3.770137^{+8.8e-05}_{-8.9e-05}$	$1817.2664^{+0.0006}_{-0.0006}$	$6.09^{+0.14}_{-0.1}$	$5.34^{+0.15}_{-0.12}$	$2.87^{+0.03}_{-0.03}$	$2.55^{+0.05}_{-0.05}$	$0.045^{+0.0004}_{-0.0004}$	n
1710.01	$24.283384^{+1.9e-05}_{-2e-05}$	$1836.9629^{+0.0005}_{-0.0006}$	$4.98^{+0.04}_{-0.04}$	$5.2^{+0.1}_{-0.09}$	$5.26^{+0.03}_{-0.02}$	$5.25^{+0.09}_{-0.1}$	$0.1655^{+0.0013}_{-0.0016}$	n
1716.01	$8.082366^{+3.5e-05}_{-3.6e-05}$	$1843.8553^{+0.0034}_{-0.0031}$	$2.17^{+0.12}_{-0.09}$	$2.88^{+0.17}_{-0.13}$	$3.51^{+0.17}_{-0.13}$	$4.45^{+0.1}_{-0.1}$	$0.0806^{+0.0009}_{-0.0009}$	n
1723.01	$13.726468^{+0.000386}_{-0.000398}$	$1852.7027^{+0.0027}_{-0.0023}$	$2.78^{+0.11}_{-0.09}$	$3.29^{+0.14}_{-0.13}$	$4.4^{+0.22}_{-0.22}$	$4.81^{+0.12}_{-0.12}$	$0.1136^{+0.0013}_{-0.0013}$	n
1726.01	$7.107941^{+7e-06}_{-6e-06}$	$1845.3735^{+0.0005}_{-0.0006}$	$2.16^{+0.05}_{-0.04}$	$2.16^{+0.06}_{-0.05}$	$3.24^{+0.04}_{-0.03}$	$3.29^{+0.05}_{-0.06}$	$0.0721^{+0.0005}_{-0.0007}$	n
1726.02	$20.543827^{+2.1e-05}_{-2.1e-05}$	$1844.0589^{+0.0006}_{-0.0006}$	$2.58^{+0.04}_{-0.04}$	$2.58^{+0.06}_{-0.04}$	$4.07^{+0.04}_{-0.04}$	$4.7^{+0.07}_{-0.08}$	$0.1462^{+0.001}_{-0.0013}$	n
1736.01	$7.073092^{+1.7e-05}_{-1.7e-05}$	$1792.7939^{+0.0018}_{-0.0019}$	$2.04^{+0.07}_{-0.05}$	$3.18^{+0.12}_{-0.1}$	$3.98^{+0.08}_{-0.08}$	$5.04^{+0.12}_{-0.11}$	$0.073^{+0.0009}_{-0.0008}$	n
1742.01	$21.269084^{+5.4e-05}_{-5.1e-05}$	$1725.352^{+0.0018}_{-0.0022}$	$1.92^{+0.03}_{-0.03}$	$2.37^{+0.06}_{-0.05}$	$6.29^{+0.07}_{-0.07}$	$5.66^{+0.12}_{-0.11}$	$0.1544^{+0.0016}_{-0.0016}$	y
1751.01	$37.468555^{+0.000141}_{-0.000138}$	$1733.6315^{+0.0028}_{-0.0029}$	$2.06^{+0.07}_{-0.04}$	$2.95^{+0.11}_{-0.08}$	$7.65^{+0.16}_{-0.1}$	$8.35^{+0.21}_{-0.19}$	$0.2145^{+0.0028}_{-0.0025}$	n
1753.01	$5.384623^{+9e-06}_{-1.1e-05}$	$1684.504^{+0.0016}_{-0.0013}$	$2.34^{+0.08}_{-0.06}$	$2.48^{+0.1}_{-0.08}$	$3.18^{+0.05}_{-0.05}$	$3.23^{+0.09}_{-0.08}$	$0.0591^{+0.0007}_{-0.0007}$	n
1758.01	$20.705061^{+4.8e-05}_{-4.8e-05}$	$1806.6981^{+0.0015}_{-0.0016}$	$4.0^{+0.25}_{-0.15}$	$3.56^{+0.23}_{-0.14}$	$3.67^{+0.1}_{-0.08}$	$4.52^{+0.11}_{-0.1}$	$0.1384^{+0.0015}_{-0.0015}$	n
1759.01	$18.850009^{+2.2e-05}_{-2.3e-05}$	$1745.4661^{+0.0009}_{-0.001}$	$4.98^{+0.17}_{-0.1}$	$3.12^{+0.12}_{-0.08}$	$3.59^{+0.09}_{-0.05}$	$3.53^{+0.04}_{-0.05}$	$0.1147^{+0.0007}_{-0.0005}$	n
1775.01	$10.240554^{+1e-05}_{-1e-05}$	$1877.5645^{+0.0005}_{-0.0005}$	$8.9^{+0.1}_{-0.09}$	$8.05^{+0.14}_{-0.13}$	$3.66^{+0.04}_{-0.03}$	$3.66^{+0.04}_{-0.04}$	$0.0898^{+0.0005}_{-0.0005}$	n
1776.01	$2.799865^{+2.5e-05}_{-3.2e-05}$	$1871.498^{+0.0038}_{-0.0037}$	$1.19^{+0.09}_{-0.07}$	$1.22^{+0.09}_{-0.08}$	$1.93^{+0.19}_{-0.18}$	$2.5^{+0.06}_{-0.05}$	$0.0378^{+0.0004}_{-0.0004}$	n
1778.01	$6.527337^{+4.4e-05}_{-4e-05}$	$1876.0046^{+0.0025}_{-0.0026}$	$2.02^{+0.12}_{-0.1}$	$2.9^{+0.19}_{-0.14}$	$2.98^{+0.18}_{-0.15}$	$4.31^{+0.05}_{-0.09}$	$0.0726^{+0.0006}_{-0.0006}$	n
1794.01	$8.765566^{+7.3e-05}_{-6.8e-05}$	$1715.309^{+0.004}_{-0.0033}$	$2.3^{+0.11}_{-0.09}$	$3.3^{+0.17}_{-0.14}$	$3.92^{+0.13}_{-0.13}$	$5.11^{+0.12}_{-0.1}$	$0.0824^{+0.0009}_{-0.0009}$	n
1797.01	$1.039141^{+5e-06}_{-3e-06}$	$1900.238^{+0.0014}_{-0.0016}$	$1.31^{+0.06}_{-0.05}$	$1.47^{+0.07}_{-0.07}$	$1.82^{+0.06}_{-0.06}$	$1.89^{+0.03}_{-0.04}$	$0.0206^{+0.0002}_{-0.0002}$	n
1797.02	$3.645143^{+8e-06}_{-8e-06}$	$1902.8746^{+0.0014}_{-0.0014}$	$2.77^{+0.11}_{-0.08}$	$3.12^{+0.14}_{-0.1}$	$2.36^{+0.06}_{-0.06}$	$2.89^{+0.05}_{-0.06}$	$0.0476^{+0.0004}_{-0.0005}$	n
1798.01	$0.437815^{+1e-06}_{-2e-06}$	$1739.0717^{+0.0}_{-0.001}$	$1.62^{+0.08}_{-0.06}$	$1.4^{+0.07}_{-0.06}$	$1.28^{+0.04}_{-0.05}$	$1.19^{+0.02}_{-0.02}$	$0.0107^{+0.0001}_{-0.0001}$	n
1798.02	$8.021543^{+2.9e-05}_{-3.3e-05}$	$1741.5941^{+0.0022}_{-0.0022}$	$2.76^{+0.13}_{-0.1}$	$2.39^{+0.12}_{-0.09}$	$3.14^{+0.11}_{-0.08}$	$3.12^{+0.04}_{-0.04}$	$0.0744^{+0.0005}_{-0.0006}$	n
1799.01	$7.085754^{+8.4e-05}_{-9.2e-05}$	$1904.8305^{+0.0084}_{-0.008}$	$1.37^{+0.09}_{-0.08}$	$1.42^{+0.09}_{-0.09}$	$3.14^{+0.18}_{-0.18}$	$3.45^{+0.08}_{-0.08}$	$0.0707^{+0.0008}_{-0.0008}$	n
1801.01	$10.643985^{+2.7e-05}_{-2.5e-05}$	$1903.5423^{+0.0013}_{-0.0014}$	$3.51^{+0.11}_{-0.11}$	$1.96^{+0.08}_{-0.08}$	$2.7^{+0.06}_{-0.05}$	$2.67^{+0.04}_{-0.04}$	$0.0754^{+0.0005}_{-0.0005}$	n
1807.01	$0.549371^{+1e-06}_{-1e-06}$	$1900.4436^{+0.0004}_{-0.0003}$	$1.84^{+0.09}_{-0.07}$	$1.5^{+0.08}_{-0.07}$	$0.98^{+0.02}_{-0.02}$	$1.23^{+0.03}_{-0.03}$	$0.0122^{+0.0001}_{-0.0001}$	n
1823.01	$38.81359^{+3.3e-05}_{-3.3e-05}$	$1715.179^{+0.0004}_{-0.0004}$	$8.59^{+0.11}_{-0.08}$	$7.54^{+0.33}_{-0.25}$	$5.92^{+0.04}_{-0.04}$	$5.72^{+0.21}_{-0.26}$	$0.2118^{+0.0022}_{-0.0023}$	n
1824.01	$22.80853^{+6e-05}_{-6.2e-05}$	$1879.5468^{+0.0013}_{-0.0012}$	$3.1^{+0.09}_{-0.07}$	$2.74^{+0.09}_{-0.07}$	$4.11^{+0.06}_{-0.05}$	$4.51^{+0.07}_{-0.08}$	$0.1508^{+0.0011}_{-0.0013}$	n
1836.01	$1.772745^{+6e-06}_{-5e-06}$	$1929.5241^{+0.0018}_{-0.0024}$	$1.45^{+0.12}_{-0.08}$	$2.6^{+0.22}_{-0.14}$	$1.79^{+0.06}_{-0.08}$	$3.46^{+0.07}_{-0.07}$	$0.0309^{+0.0002}_{-0.0003}$	n
1836.02	$20.380831^{+2.5e-05}_{-2.7e-05}$	$1933.166^{+0.0008}_{-0.0008}$	$4.61^{+0.07}_{-0.06}$	$8.28^{+0.2}_{-0.17}$	$6.62^{+0.07}_{-0.05}$	$7.97^{+0.16}_{-0.16}$	$0.1574^{+0.001}_{-0.0017}$	n
1842.01	$9.573924^{+1.5e-05}_{-1.5e-05}$	$1933.3359^{+0.0009}_{-0.0009}$	$5.57^{+0.07}_{-0.07}$	$12.35^{+0.28}_{-0.29}$	$4.31^{+0.08}_{-0.07}$	$7.32^{+0.16}_{-0.15}$	$0.1002^{+0.0007}_{-0.0008}$	n
1898.01	$45.522288^{+6.1e-05}_{-6.2e-05}$	$1894.252^{+0.0007}_{-0.0007}$	$5.34^{+0.09}_{-0.14}$	$9.4^{+0.23}_{-0.31}$	$4.27^{+0.06}_{-0.06}$	$10.28^{+0.22}_{-0.19}$	$0.2687^{+0.0019}_{-0.0027}$	n
2019.01	$15.32222^{+0.000181}_{-0.000172}$	$1942.9799^{+0.0042}_{-0.0054}$	$2.8^{+0.13}_{-0.1}$	$5.33^{+0.26}_{-0.21}$	$7.57^{+0.24}_{-0.26}$	$7.67^{+0.26}_{-0.13}$	$0.1277^{+0.0038}_{-0.0009}$	n
2045.01	$9.077535^{+8.5e-05}_{-8.4e-05}$	$1765.5949^{+0.0014}_{-0.0014}$	$6.59^{+0.12}_{-0.1}$	$12.77^{+0.36}_{-0.34}$	$5.9^{+0.09}_{-0.08}$	$6.62^{+0.16}_{-0.16}$	$0.0927^{+0.0008}_{-0.0019}$	n
2076.01	$10.355307^{+1.4e-05}_{-1.5e-05}$	$1743.724^{+0.001}_{-0.0009}$	$3.19^{+0.12}_{-0.07}$	$2.77^{+0.14}_{-0.1}$	$3.24^{+0.05}_{-0.04}$	$3.44^{+0.09}_{-0.12}$	$0.0883^{+0.0007}_{-0.0007}$	y
2076.02	$21.015324^{+2.3e-05}_{-2.4e-05}$	$1748.6895^{+0.0006}_{-0.0006}$	$4.26^{+0.06}_{-0.05}$	$3.69^{+0.14}_{-0.09}$	$4.19^{+0.04}_{-0.03}$	$4.4^{+0.12}_{-0.16}$	$0.1415^{+0.0011}_{-0.0012}$	y
2076.03	$35.125611^{+9.6e-05}_{-8.5e-05}$	$1762.6658^{+0.0016}_{-0.0019}$	$3.95^{+0.2}_{-0.27}$	$3.43^{+0.21}_{-0.25}$	$2.97^{+0.12}_{-0.09}$	$5.2^{+0.14}_{-0.18}$	$0.1993^{+0.0016}_{-0.0016}$	n
2088.01	$124.730182^{+0.00061}_{-0.000575}$	$1769.6077^{+0.0031}_{-0.0032}$	$3.98^{+0.13}_{-0.1}$	$3.68^{+0.19}_{-0.14}$	$7.36^{+0.15}_{-0.14}$	$8.32^{+0.27}_{-0.36}$	$0.4722^{+0.0039}_{-0.0044}$	n
2114.01	$6.209837^{+0.000206}_{-0.000197}$	$2719.047^{+0.0011}_{-0.0011}$	$6.17^{+0.07}_{-0.08}$	$14.1^{+0.33}_{-0.32}$	$4.6^{+0.08}_{-0.08}$	$6.55^{+0.11}_{-0.13}$	$0.0753^{+0.0005}_{-0.0006}$	n
2128.01	$16.341418^{+0.000145}_{-0.000128}$	$1987.2651^{+0.0022}_{-0.0022}$	$1.71^{+0.06}_{-0.05}$	$2.09^{+0.09}_{-0.08}$	$4.7^{+0.14}_{-0.11}$	$5.22^{+0.14}_{-0.13}$	$0.1271^{+0.0016}_{-0.0016}$	n
2145.01	$10.261125^{+1.1e-05}_{-1.2e-05}$	$2013.2802^{+0.0006}_{-0.0006}$	$4.14^{+0.05}_{-0.04}$	$12.42^{+0.31}_{-0.25}$	$7.47^{+0.05}_{-0.04}$	$9.52^{+0.21}_{-0.19}$	$0.1107^{+0.0007}_{-0.0009}$	n

Note. Properties of 108 planets orbiting the 85-star TKS sample. Orbital period P, transit midpoint t_0 (given in BTJD = BJD $-2{,}457{,}000$), transit duration T_{14}, and planet-to-star radius ratio $R_p/R_\star$ were measured from a final fit using `exoplanet` (Foreman-Mackey et al. 2021) and reweighted via importance sampling. The given values reflect median measurements with upper and lower uncertainties. R_p follows from $R_p/R_\star$ and $R_\star$. The expected duration of a centrally transiting object on a circular orbit T_{circ} and semimajor axis a are determined from Kepler's third law (Winn 2010). The last column shows a flag (yes or no) indicating whether or not observed TTVs are significant for a given planet.

(This table is available in machine-readable form.)

method has been found to produce biased results (see Gilbert et al. 2022), the latter is unbiased but requires three parameters to measure that which can be described by one (T_{14}) more efficiently. Our duration-sampling method also allows us to calculate posterior distributions for e and ω post-modeling through importance sampling, described further in Section 4. Regardless of the method used, we emphasize that most $\{e, \omega\}$ constraints measured from photometry alone are imprecise for individual planets and are better applied toward population-level studies (Section 5.4).

We sample the posterior probability density of all model parameters with exoplanet using the gradient-based No U-Turn Sampling method (Hoffman & Gelman 2011; Betancourt 2016) as implemented by PyMC3 (Salvatier et al. 2016). For all posterior sampling performed in this work, we use 5000 tuning steps with an additional 3000 sampler draws and a target acceptance fraction of 0.95. This sampling process is performed via two sampler chains across two CPU cores, and we consider the process to be converged when the Gelman–Rubin statistic $\hat{R}$ for these chains is $\hat{R} < 1.01$ (Gelman & Rubin 1992).

4. Planet Properties

4.1. Importance-weighted Posterior Distributions

Our final planet property measurements are based on the posterior distributions measured with exoplanet. These properties are modeled via a fit to the transit shape, conditioned on the input light-curve data. However, our selected modeling basis does not inherently assume that any information is known about $\rho_\star$, e, or ω, and therefore the posterior chains produced directly by our sampler can be considered unweighted. Given our robust measurements of $\rho_\star$ from our stellar characterization, we can apply an "importance weight" (Oh & Berger 1993; Gilks et al. 1995) to these posterior samples according to how well the unweighted results can be described by the $\rho_\star$ values measured with isoclassify. We will refer to these precise stellar density measurements as $\rho_{\star,\mathrm{iso}}$. The importance weights also allow us to produce properly weighted posterior distributions for e and ω without needing to directly sample them during the light-curve modeling—a step that takes seconds rather than hours. This method has been used extensively in past literature for similar applications of improving modeling efficiency (see, e.g., Ford 2005, 2006) or measuring eccentricity (see, e.g., Dawson & Johnson 2012; Van Eylen et al. 2019).

To determine the appropriate importance weights, we first calculate the estimated stellar density at each sampler step based on the sampled quantities P, $R_p/R_\star$, b, and T_{14}. We refer to this derived density as $\rho_{\star,\mathrm{derived}}$. We calculate these values according to Equation (1), which is a rearrangement of the transit duration equation described by Winn (2010):

$$\rho_{\star,\mathrm{derived}} = \frac{3\pi}{GP^2}\left(\frac{(1 + R_p/R_\star)^2 - b^2}{\sin^2\left(\frac{T_{14}\pi}{P}\frac{1 + e\sin\omega}{\sqrt{1 - e^2}}\right)} + b^2\right)^{3/2}. \quad (1)$$

This equation, however, also includes e and ω, for which we do not yet have any information. Here we draw random samples of $\{e, \omega\}$ from uniform prior distributions $e \sim U(0, 1)$ and $\omega \sim U(-\frac{\pi}{2}, \frac{3\pi}{2})$ to be used in the calculation. We prefer to use

uninformative uniform priors on these parameters to remain agnostic to eccentricity here but will explore the parameterization of this eccentricity prior more in depth in M. MacDougall et al. (2023, in preparation). The stellar density values that we calculate here produce a derived posterior distribution based on our unweighted posterior samples and uniform $\{e, \omega\}$ samples.

We then compare the samples of $\rho_{\star,\mathrm{derived}}$ against the independently measured $\rho_{\star,\mathrm{iso}}$ for a given target by computing the log-likelihood of each ith sample,

$$\log\mathcal{L}_i = -\frac{1}{2}\left(\frac{\rho_{\star,\mathrm{derived},i} - \rho_{\star,\mathrm{iso}}}{\sigma(\rho_{\star,\mathrm{iso}})}\right)^2, \quad (2)$$

assuming a Gaussian likelihood function. We then weight each sample from our original unweighted posterior distributions by

$$w_i = \frac{\mathcal{L}_i}{\sum_i \mathcal{L}_i} \quad (3)$$

to produce the final importance-weighted posterior distributions for each parameter. We also apply these same weights to the random, uniform $\{e, \omega\}$ samples to derive their weighted posterior distributions. All summary statistics that are reported or used throughout the remaining analysis are based on the 15th, 50th, and 85th percentiles of these importance-weighted posteriors.
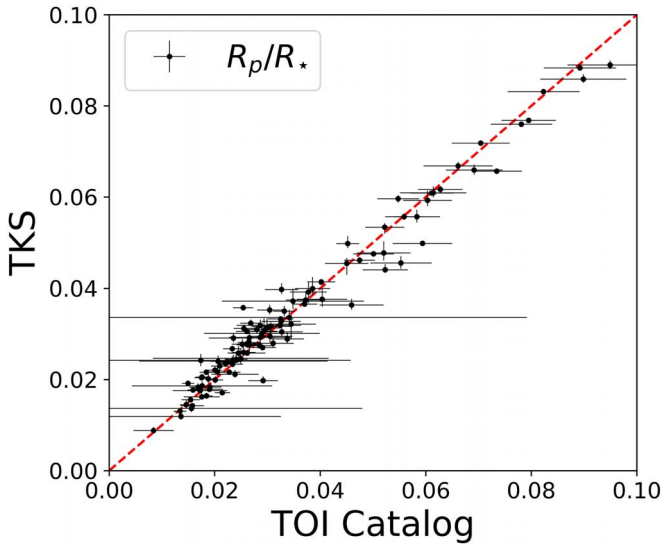
4.2. Planet-to-star Radius Ratio

Before deriving final planet radii, we first confirm that our final modeled $R_p/R_\star$ values are unbiased and generally consistent with those reported by the TOI Catalog (Figure 5). We find no evidence of systematic bias in our results, measuring the average ratio between the TKS results and TOI Catalog values $(R_p/R_\star)_{\mathrm{TKS}}/(R_p/R_\star)_{\mathrm{TOI}} = 1.02 \pm 0.11$. This is consistent within the average fractional uncertainty of $R_p/R_\star$ from the TOI Catalog. We show the residuals of this comparison, $((R_p/R_\star)_{\mathrm{TKS}} - (R_p/R_\star)_{\mathrm{TOI}})/\sigma(R_p/R_\star)_{\mathrm{TOI}}$, in Figure 6(b). Here we see that 4 out of 108 TKS planets have $(R_p/R_\star)_{\mathrm{TKS}}$ measurements that are $\gtrsim 3\sigma_{\mathrm{TOI}}$ discrepant from $(R_p/R_\star)_{\mathrm{TOI}}$.

Upon closer inspection, we find that these discrepancies occur in instances where our careful detrending and TTV modeling led to more reliable $R_p/R_\star$ measurements. An example of this can be seen in Figure 4, where the initial PDC-SAP photometry of TOI-1136 displays significant variability, which we remove before performing our final transit fits that include TTV modeling. Our measured $R_p/R_\star$ values are consistent within $\sim 1.5\sigma$ of the published values reported by Dai et al. (2023), while the $R_p/R_\star$ values reported by the TOI Catalog are far more discrepant.

4.3. Derived Planet Properties

We calculate the radius of each planet in our sample (R_p) from our final weighted posterior distributions of $R_p/R_\star$ and our isochrone-modeled $R_\star$ values. When compared against the TOI Catalog measurements, we find that our planet radii have a lower median uncertainty, reduced from $\sigma(R_p)/R_p \approx 6.7\%$ for TOI Catalog values to 3.8% for TKS results. When looking at the mean uncertainty rather than the median, the difference is even more significant owing to large outliers among the SPOC

Figure 5. Planet-to-star radius ratio $R_p/R_\star$ as measured by our planet characterization pipeline (TKS; *y*-axis) compared to the radius ratio values reported by the TOI Catalog (*x*-axis). The TKS results have significantly reduced uncertainties and are generally consistent with the TOI Catalog results (see Section 4.2).

pipeline outputs, with mean uncertainties reduced from $\sigma(R_p)/R_p \approx 16.1\%$ to 3.9%.

The planet radius distribution that we measure for the TKS sample is shown in Figure 7, displayed against the distribution of TKS planet radii reported by the TOI Catalog. We show the residuals of this comparison, $(R_{p,\mathrm{TKS}} - R_{p,\mathrm{TOI}})/\sigma(R_{p,\mathrm{TOI}})$, in Figure 6(c). We observe similar residual distributions for both $R_p/R_\star$ and R_p but far less significant scatter in the $R_\star$ residuals (Figure 6(a)), suggesting that the uncertainties on R_p are dominated by differences in light-curve modeling rather than stellar characterization (Petigura 2020).

Along with planet radii, we also compute semimajor axis a, incident stellar flux S_{inc}, and equilibrium temperature T_{eq} for each planet. We calculate these parameters assuming constant planet-to-star separation, which is not a valid approximation for eccentric orbits, so these values should only be considered as estimates in such cases. We compute semimajor axes from Kepler's third law, using precise values of P and our well-constrained measurements of $M_\star$. The median uncertainty among these measurements is $\sigma(a)/a \approx 1\%$. We also calculate S_{inc} and T_{eq} using the standard equations described in Johnson et al. (2017), assuming a Bond albedo of $\alpha = 0.3$, which is typical of a super-Earth-size Kepler planet (Demory 2014). This assumption is not uniformly applicable across our sample, but it is a common simplification among similar studies such as the CKS (Johnson et al. 2017). The median uncertainties that we measure for S_{inc} and T_{eq} are 6.7% and 1.7%, respectively, without accounting for the uncertainty in α.

5. Discussion

5.1. Radius Gap

We note from Chontos et al. (2022) that a primary goal of TKS Science Case 1A is to better understand the bimodal distribution of small-planet radii first described by Fulton et al. (2017). This radius valley has been studied extensively from both Kepler and K2 planets (see, e.g., Berger et al. 2018; Cloutier & Menou 2020), which have improved our

understanding of the physical mechanisms leading to this phenomenon (Van Eylen et al. 2018; Gupta & Schlichting 2019). For the first time among TESS planets, we observe a valley-like structure between 1.5 and 2.0 $R_\oplus$ among the TKS sample. In Figure 7, we show the distribution of TKS planet radii and highlight the radius valley, which we find is insensitive to differences in binning. We also find this structure to be more significant among our precisely measured TKS radii from this work as compared to the TOI Catalog radii. We attribute this difference primarily to our improved constraints on $R_p/R_\star$ from our light-curve detrending and modeling procedure (see, e.g., Petigura 2020).

The radius gap has also been found to have some reliance on various other system properties such as orbital period, incident flux (Cloutier & Menou 2020), and stellar parameters as well (Fulton & Petigura 2018; Berger et al. 2020b; Chen et al. 2022). This was recently explored by Petigura et al. (2022) for the sample of 1246 planets in the CKS (Petigura et al. 2017b), which was the Kepler-focused predecessor to the TESS-Keck Survey. Although the TKS planet sample is only 8.4% the size of the CKS sample, our results do suggest the existence of a radius valley in various 2D representations of radius as a function of other parameters: $R_p - P$, $R_p - S_{\mathrm{inc}}$, $R_p - M_\star$, and R_p–[Fe/H] (Figure 8). The orange shaded regions in these figures show the radius valley as measured by Petigura et al. (2022) in the various parameter spaces, which generally agree with our results despite the CKS and TKS samples having different selection criteria. Future investigations into the radius valley may combine these samples to gain further insight to the mechanisms driving the apparent bimodality in the distribution of small-planet radii.

5.2. Hot Neptune Desert

Similar to the radius gap, the Hot Neptune Desert has been proposed as a region of $R_p - P$ parameter space that is sparsely populated, with few Neptune-size planets at $P \lesssim 5$ days. The mechanism that would drive such an effect is currently unknown, but this sparsity has been proposed as a natural consequence of photoevaporation (Lopez & Fortney 2013; Owen & Wu 2013). The Hot Neptune Desert region can be seen in Figure 8(a), outlined by boundaries defined by Mazeh et al. (2016). We find that the TKS sample includes at least 12 planets that fall firmly within this region (see, e.g., MacDougall et al. 2022; Van Zandt et al. 2023), supplying future investigations with an increased sample size to better understand the nature of the Hot Neptune Desert. Further studies will be carried out by the TKS team to determine the compositions (TKS Science Case 1B) and atmospheric properties (TKS Science Case 3) of such TKS planets to probe this topic further with planet masses retrieved from ongoing RV measurements.

5.3. Multiplanet Systems and TTVs

The TKS sample was selected to contain several systems with multiple transiting planet signals, fulfilling TKS Science Case 2C. Among our 85 target systems, we report 69 with a single transiting planet signal, 11 with two transit signals, 3 with three transit signals (TOI-561, Weiss et al. 2021; TOI-1339, Lubin et al. 2022; TOI-2076, Osborn et al. 2022), 1 with four transit signals (TOI-1246; Turtelboom et al. 2022), and 1 with more than four transit signals (TOI-1136). For TOI-1136,
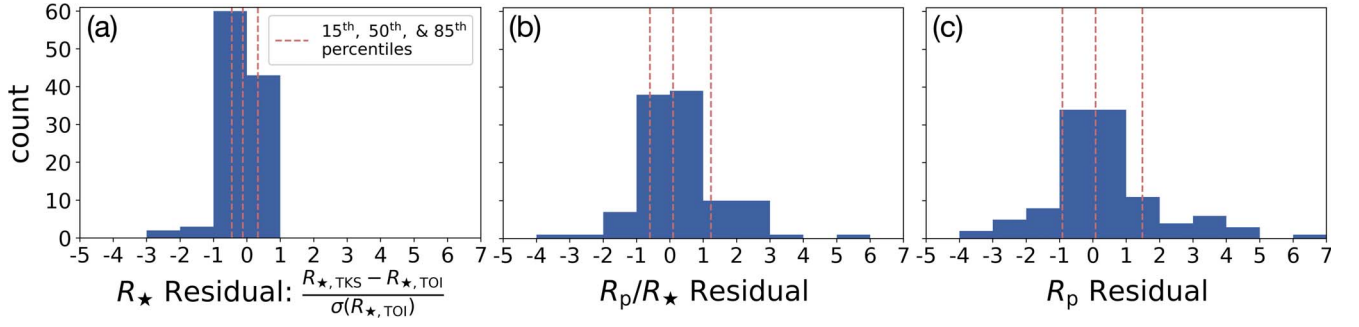
Figure 6. Residuals of (a) stellar radius $R_\star$, (b) planet-to-star radius ratio $R_p/R_\star$, and (c) planet radius R_p between our results and the TOI Catalog measurements (i.e., residual $= (R_{\star,\mathrm{TKS}} - R_{\star,\mathrm{TOI}})/\sigma(R_{\star,\mathrm{TOI}})$). Dashed vertical lines show the 15th, 50th, and 85th percentiles of each distribution of residuals.
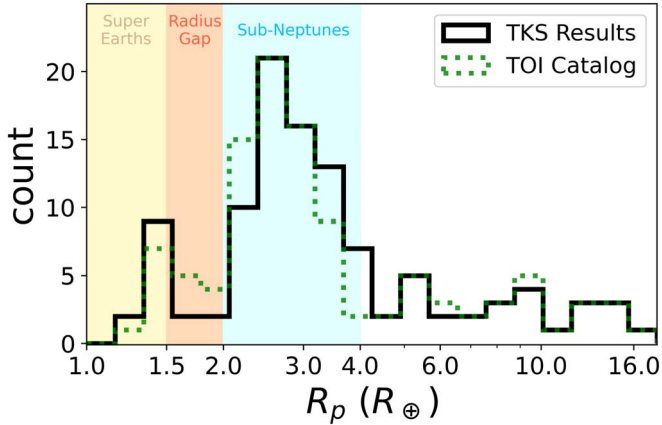
Figure 7. Distribution of median planet radius measurements for the TKS sample from this work, compared against the median radii taken from the TOI Catalog (green). Shaded regions show specific planet categories, classified by planetary radius. We observe a sparser radius gap region using TKS results than is implied by radii from the TOI Catalog, likely owing to our higher-precision measurements.

we only report on four transiting planets in this work, but ongoing investigations by TKS collaborators are working toward revealing the true number of transiting planets in this system (see Dai et al. 2023). We also measure orbital periods in some multiplanet systems that differ from those reported by the SPOC pipeline. These include TOI-561.03 (see Lacedelli et al. 2022), TOI-266.02 (J. Akana Murphy et al. 2023, in preparation[23]), and TOI-1471.02 (H. Osborn et al. 2023, in preparation). Our findings thus help to better resolve the architectures of several multiplanet systems. These systems are discussed further in the literature, verifying the results of our analysis.

We also note that several of the multiplanet systems in our sample display resonant or near-resonant orbital configurations, such as the 1:2 orbital period ratios among the inner planets in the TOI-1136 system (see Dai et al. 2023), as well as the outer planets in the TOI-1246 system (Turtelboom et al. 2022). Such orbital configurations can give rise to significant TTVs, which we observe for TOI-1136.01 and TOI-1246.03 with TTV semiamplitudes of ~24 and ~61 minutes, respectively (Figures 9(a), (b)). The resonant counterparts to these two planets, TOI-1136.02 and TOI-1246.04, also display significant

TTVs with similar semiamplitudes to their companions but with possible anticorrelation and less distinguishable periodicity. We assert that our measured TTVs for a given planet are significant when >32% of the measured transit times differ from a linear ephemeris by >1σ.

The near-resonant planets in the TOI-2076 system also display possibly significant TTVs, as first noted by Osborn et al. (2022), but we do not identify a clear structure to this signal. Additionally, we observe possible TTV chopping for TOI-1339.03 (TTV semiamplitude ≈22 minutes; Figure 9(d)), which orbits near the 3:4 mean-motion resonance with TOI-1339.02 (TTV semiamplitude ≈10 minutes), as suggested by Badenas-Agusti et al. (2020). The semiamplitudes that we report here are only an approximation, estimated as half the difference between the maximum and minimum TTV value for a given planet.

It is also possible for TTVs to arise in systems without a known transiting companion, suggesting the presence of an additional nontransiting planet. Although most single-planet orbits among the TKS sample can be described by a linear ephemeris (see Section 3.4), we identify at least one planet that displays significant TTVs without a known companion: TOI-1279.01 with a TTV semiamplitude of ~34 minutes (Figure 9(c)). At least two other single-planet systems among the TKS sample also display possible TTVs, TOI-1611.01 and TOI-1742.01, but these signals are less significant relative to the other TTV systems described above. The dynamics and multiplicities of the TKS systems discussed in this section will be examined further in future TKS studies of multiplanet systems (TKS Science Case 2C) and distant giant companions (TKS Science Case 2A).

5.4. Eccentricity

Through importance sampling (Section 4.1), we measure posterior distributions for e and ω for all planets in the TKS sample using stellar density and the results of our photometric modeling. The goal of TKS Science Case 2Bi is to characterize the eccentricities of sub-Jovian planets and better measure their underlying eccentricity distribution. Generally, however, photometric modeling alone is known to produce imprecise measurements of $\{e, \omega\}$ on a planet-by-planet basis. Since ω is typically unconstrained from transits and b is often loosely constrained for small planets owing to ambiguous ingress/egress signals, strong covariances between b, e, and ω drive large uncertainties in photometrically derived eccentricities. We observe this with sub-Neptune TOI-1255.01 from the TKS sample (MacDougall et al. 2021), for which the photometric

---

[23] Period ambiguity resolved via private communications with the CHEOPS team (point of contact: Hugh Osborn).
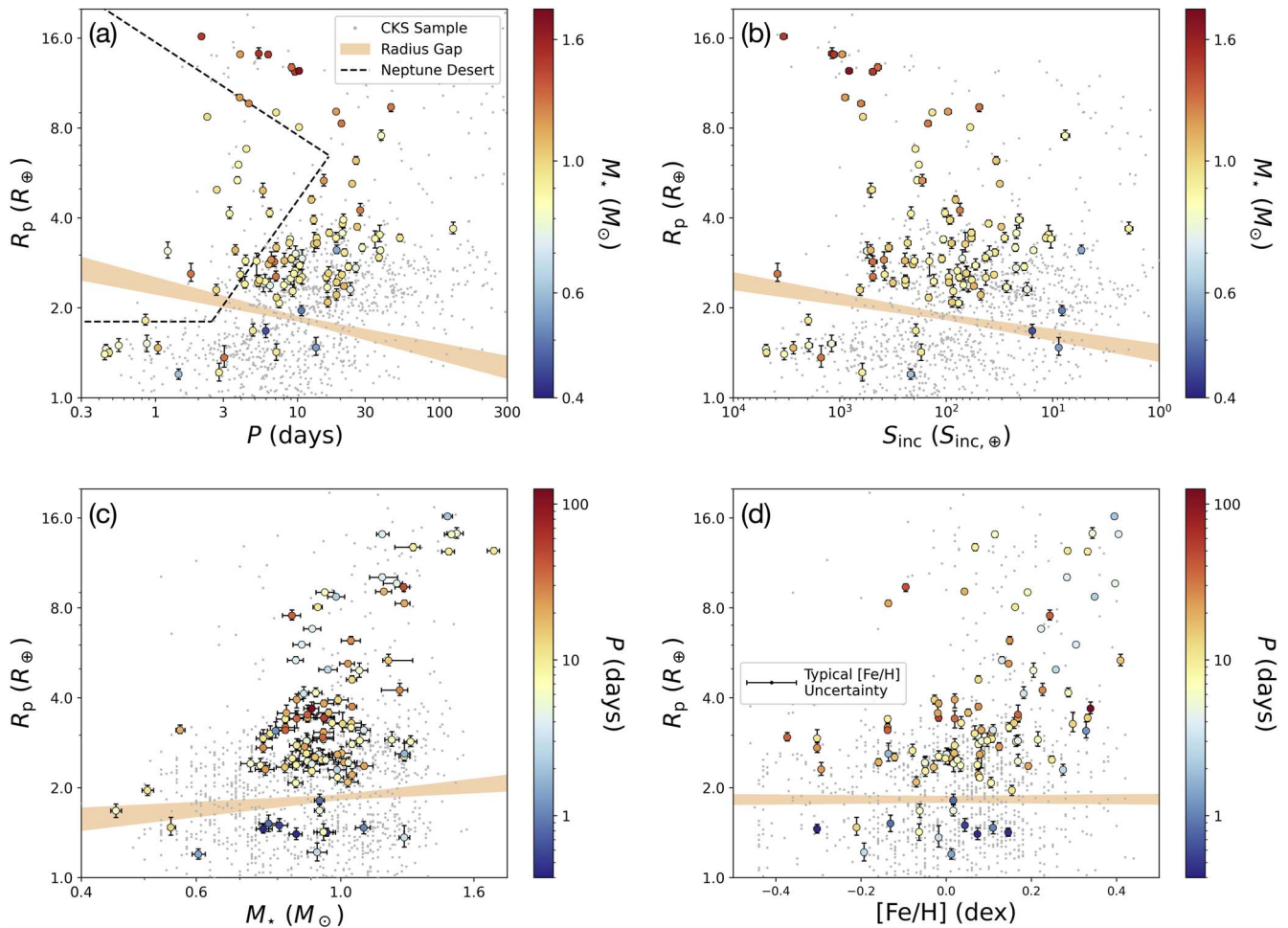
Figure 8. (a) Radius and orbital period for all TKS planets, with stellar mass shown as a color scale. Gray background points show the distribution of planets from the CKS sample (Petigura et al. 2022). The radius gap, as defined by Petigura et al. (2022), is shown as the orange shaded region. The Hot Neptune Desert, as defined by Mazeh et al. (2016), is shown as the region marked off by black dashed lines. (b) Same as panel (a), except x-axis is S_{inc}. (c) Same as panel (a), except x-axis is $M_\star$ and color scale is P. (d) Same as panel (c), except x-axis is [Fe/H].

eccentricity e_{phot} was highly degenerate with b until additional eccentricity constraints were introduced from RV measurements to determine $e \approx 0.16$. On the other hand, we also identified the Neptune-size TKS target TOI-1272.01 (MacDougall et al. 2022) as moderately eccentric based on e_{phot} and later confirmed a self-consistent eccentricity of $e \approx 0.34$ via joint modeling with RVs.

Rather than using our photometrically derived eccentricities to draw conclusions about planets on an individual level, we are conducting an ongoing study to determine the population-level eccentricity distribution underlying the TKS sample (M. MacDougall et al. 2023, in preparation). In this way, we are less sensitive to parameter covariances like b-e-ω and other effects like the Lucy−Sweeney bias, which leads to preferentially noncircular orbit fits (Lucy & Sweeney 1971; Eastman et al. 2013). An investigation is also underway by members of TKS to measure more precise eccentricities for planets in our sample using RV measurements (A. Polanski et al. 2023, in preparation), which will aid in breaking the degeneracy between e and b for lower-S/N planets.

6. Conclusions

In this work, we characterized 85 TESS target stars presented by Chontos et al. (2022) as the TESS-Keck Survey sample.

Through a combination of photometry, high-resolution spectroscopy, and Gaia parallaxes, we measured stellar properties for these targets with improved precision relative to past works. We used these stellar characterizations to facilitate in homogeneously modeling the light-curve photometry of each TKS target, including fitting for photometric variability, estimating transit times, and measuring the transit properties of planet candidates recovered from the reduced light-curve photometry. We characterized a total of 108 transiting planet candidates orbiting the 85 TKS target stars —the largest sample of homogeneously characterized planets from the TESS mission to date.

In measuring the radii of these planets, we found a substantial increase in precision among our radii relative to the TOI Catalog ($\sigma(R_{p,TOI})/R_{p,TOI} \approx 6.7\%$ vs. $\sigma(R_{p,TKS})/R_{p,TKS} \approx 3.8\%$), largely attributed to our improved accuracy in measuring $R_p/R_\star$. From our updated radii, we successfully recovered the radius gap in both one-dimensional (R_p) and two-dimensional ($R_p - P$, $R_p - S_{inc}$, $R_p - M_\star$, and R_p–[Fe/H]) parameter spaces. While we do not provide new models to fit the topology of the radius gap in these parameter spaces, we find that the distribution of radii in the radius gap region is broadly consistent with that of Kepler planets. We also identify significant TTVs among several TKS systems, including multiplanet systems TOI-1136, TOI-
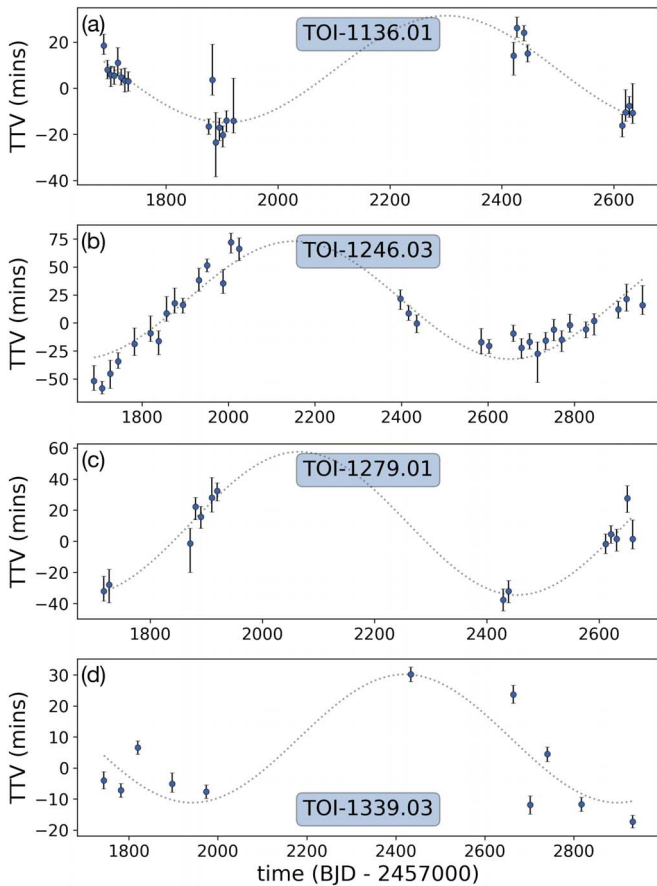
Figure 9. Four examples of significant TTVs detected among TKS systems, including three from multiplanet systems (panels (a), (b), and (d)) and one from a single-planet system (panel (c)). (a) TOI-1136.01: TTV semiamplitude ≈24 minutes, TTV signal period ≈790 days; (b) TOI-1246.03: TTV semiamplitude ≈61 minutes, TTV signal period ≈990 days; (c) TOI-1279.01: TTV semiamplitude ≈34 minutes, TTV signal period ≈775 days; (d) TOI-1339.03: TTV semiamplitude ≈22 minutes, TTV signal period ≈960 days, with significant scatter likely attributed to TTV chopping. These TTVs are measured from the observed transit midpoints (fit via `exoplanet`) minus the transit midpoints calculated assuming a linear ephemeris. An estimated sinusoidal signal is shown fit to each set of TTVs, using a Lomb−Scargle periodogram and regression fit from `astropy`. These significant TTV signals likely arise from dynamical interactions between planetary companions.

1246, and TOI-1339, as well as the single-planet system TOI-1279. These TTVs will inform future investigations into the dynamics and multiplicity of TKS systems.

The TKS Collaboration will continue to use the planetary and stellar characterizations from this work to answer key questions that remain in the field of exoplanet science, covering the topics of bulk planet compositions, system architectures and dynamics, planet atmospheres, and the effects of stellar evolution. Our photometric analysis will soon be accompanied by an RV analysis of all TKS targets as well (A. Polanski et al. 2023, in preparation), which will provide us with new planetary system characteristics such as planet masses, precise eccentricities, and discoveries of nontransiting planets. The combination of insights from the photometry described here and upcoming RV measurements will allow us to more fully answer the questions laid out by the TKS Science Cases.

The stellar and planetary properties measured from this work are summarized in Tables 3 and 4. This data is also available in machine-readable format on GitHub, along with additional

Software: We made use of the following publicly available Python modules: `exoplanet` (Foreman-Mackey et al. 2021),

---

PyMC3 (Salvatier et al. 2016), theano (The Theano Development Team et al. 2016), celerite2 (Foreman-Mackey 2018), astropy (Astropy Collaboration et al. 2013, 2018), isoclassify (Huber et al. 2017), light-kurve (Lightkurve Collaboration et al. 2018), matplotlib (Hunter 2007), numpy (Harris et al. 2020), scipy (Virtanen et al. 2020), limb-darkening (Espinoza & Jordán 2015), SpecMatch-Synth (Petigura et al. 2017a), SpecMatch-Emp (Yee et al. 2017), and pandas (McKinney 2010).

ORCID iDs

Mason G. MacDougall ⓘ https://orcid.org/0000-0003-2562-9043
Erik A. Petigura ⓘ https://orcid.org/0000-0003-0967-2893
Gregory J. Gilbert ⓘ https://orcid.org/0000-0003-0742-1660
Isabel Angelo ⓘ https://orcid.org/0000-0002-9751-2664
Natalie M. Batalha ⓘ https://orcid.org/0000-0002-7030-9519
Corey Beard ⓘ https://orcid.org/0000-0001-7708-2364
Aida Behmard ⓘ https://orcid.org/0000-0003-0012-9093
Sarah Blunt ⓘ https://orcid.org/0000-0002-3199-2888
Casey Brinkman ⓘ https://orcid.org/0000-0002-4480-310X
Ashley Chontos ⓘ https://orcid.org/0000-0003-1125-2564
Ian J. M. Crossfield ⓘ https://orcid.org/0000-0002-1835-1891
Fei Dai ⓘ https://orcid.org/0000-0002-8958-0683
Paul A. Dalba ⓘ https://orcid.org/0000-0002-4297-5506
Courtney Dressing ⓘ https://orcid.org/0000-0001-8189-0233
Tara Fetherolf ⓘ https://orcid.org/0000-0002-3551-279X
Benjamin Fulton ⓘ https://orcid.org/0000-0003-3504-5316
Steven Giacalone ⓘ https://orcid.org/0000-0002-8965-3969
Michelle L. Hill ⓘ https://orcid.org/0000-0002-0139-4756
Rae Holcomb ⓘ https://orcid.org/0000-0002-5034-9476
Andrew W. Howard ⓘ https://orcid.org/0000-0001-8638-0320
Daniel Huber ⓘ https://orcid.org/0000-0001-8832-4488
Howard Isaacson ⓘ https://orcid.org/0000-0002-0531-1073
Stephen R. Kane ⓘ https://orcid.org/0000-0002-7084-0529
Jack Lubin ⓘ https://orcid.org/0000-0001-8342-7736
Teo Močnik ⓘ https://orcid.org/0000-0003-4603-556X
Joseph M. Akana Murphy ⓘ https://orcid.org/0000-0001-8898-8284
Daria Pidhorodetska ⓘ https://orcid.org/0000-0001-9771-7953
Alex S. Polanski ⓘ https://orcid.org/0000-0001-7047-8681
Malena Rice ⓘ https://orcid.org/0000-0002-7670-670X
Paul Robertson ⓘ https://orcid.org/0000-0003-0149-9678
Lee J. Rosenthal ⓘ https://orcid.org/0000-0001-8391-5182
Arpita Roy ⓘ https://orcid.org/0000-0001-8127-5775
Ryan A. Rubenzahl ⓘ https://orcid.org/0000-0003-3856-3143
Nicholas Scarsdale ⓘ https://orcid.org/0000-0003-3623-7280
Emma V. Turtelboom ⓘ https://orcid.org/0000-0002-1845-2617
Dakotah Tyler ⓘ https://orcid.org/0000-0003-0298-4667
Judah Van Zandt ⓘ https://orcid.org/0000-0002-4290-6826
Lauren M. Weiss ⓘ https://orcid.org/0000-0002-3725-3058
Samuel W. Yee ⓘ https://orcid.org/0000-0001-7961-3907

References

Andrae, René, Fouesneau, Morgan, Creevey, Orlagh, et al. 2018, A&A, 616, A8
Astropy Collaboration, Price-Whelan, A. M., Sipőcz, B. M., et al. 2018, AJ, 156, 123
Astropy Collaboration, Robitaille, T. P., Tollerud, E. J., et al. 2013, A&A, 558, A33
Badenas-Agusti, M., Günther, M. N., Daylan, T., et al. 2020, AJ, 160, 113
Bailer-Jones, C. A. L., Andrae, R., Arcay, B., et al. 2013, A&A, 559, A74
Berger, T. A., Huber, D., Gaidos, E., & van Saders, J. L. 2018, ApJ, 866, 99
Berger, T. A., Huber, D., Gaidos, E., van Saders, J. L., & Weiss, L. M. 2020b, AJ, 160, 108
Berger, T. A., Huber, D., van Saders, J. L., et al. 2020a, AJ, 159, 280
Betancourt, M. 2016, arXiv:1601.00225
Borucki, W. J., Koch, D., Basri, G., et al. 2010, Sci, 327, 977
Cacciapuoti, L., Kostov, V. B., Kuchner, M., et al. 2022, MNRAS, 513, 102
Caldwell, D. A., Tenenbaum, P., Twicken, J. D., et al. 2020, RNAAS, 4, 201
Castelli, F., & Kurucz, R. L. 2003, in IAU Symp. 210, Modelling of Stellar Atmospheres, ed. N. Piskunov, W. W. Weiss, & D. F. Gray (San Francisco, CA: ASP), A20
Chen, D.-C., Xie, J.-W., Zhou, J.-L., et al. 2022, AJ, 163, 249
Choi, J., Dotter, A., Conroy, C., et al. 2016, ApJ, 823, 102
Chontos, A., Murphy, J. M. A., MacDougall, M. G., et al. 2022, AJ, 163, 297
Claret, A., & Bloemen, S. 2011, A&A, 529, A75
Cloutier, R., & Menou, K. 2020, AJ, 159, 211
Coelho, P., Barbuy, B., Meléndez, J., Schiavon, R. P., & Castilho, B. V. 2005, A&A, 443, 735
Dai, F., Masuda, K., Beard, C., et al. 2023, AJ, 165, 33
Dai, F., Roy, A., Fulton, B., et al. 2020, AJ, 160, 193
Dalba, P. A., Gupta, A. F., Rodriguez, J. E., et al. 2020, AJ, 159, 241
Dalba, P. A., Kane, S. R., Dragomir, D., et al. 2022, AJ, 163, 61
Dawson, R. I., & Johnson, J. A. 2012, ApJ, 756, 122
Demory, B.-O. 2014, ApJL, 789, L20
Dotter, A. 2016, ApJS, 222, 8
Eastman, J., Gaudi, B. S., & Agol, E. 2013, PASP, 125, 83
Espinoza, N., & Jordán, A. 2015, MNRAS, 450, 1879
ExoFOP 2019, Exoplanet Follow-up Observing Program—TESS, IPAC, doi:10.26134/EXOFOP3
Ford, E. B. 2005, AJ, 129, 1706
Ford, E. B. 2006, ApJ, 642, 505
Foreman-Mackey, D. 2018, RNAAS, 2, 31
Foreman-Mackey, D., Luger, R., Agol, E., et al. 2021, JOSS, 6, 3285
Fulton, B. J., & Petigura, E. A. 2018, AJ, 156, 264
Fulton, B. J., Petigura, E. A., Howard, A. W., et al. 2017, AJ, 154, 109
Gelman, A., & Rubin, D. B. 1992, StaSc, 7, 457
Gilbert, G. J., MacDougall, M. G., & Petigura, E. A. 2022, AJ, 164, 92
Gilks, W., Richardson, S., & Spiegelhalter, D. 1995, Markov Chain Monte Carlo in Practice (London: Chapman & Hall) http://books.google.com/books?id=TRXrMWY_i2IC
Guerrero, N. M., Seager, S., Huang, C. X., et al. 2021, ApJS, 254, 39
Gupta, A., & Schlichting, H. E. 2019, MNRAS, 487, 24
Harris, C. R., Millman, K. J., van der Walt, S. J., et al. 2020, Natur, 585, 357
Hauschildt, P. H., & Baron, E. 1999, JCoAM, 109, 41
Hoffman, M. D., & Gelman, A. 2011, arXiv:1111.4246
Howell, S. B., Sobeck, C., Haas, M., et al. 2014, PASP, 126, 398
Huber, D., Zinn, J., Bojsen-Hansen, M., et al. 2017, ApJ, 844, 102
Hunter, J. D. 2007, CSE, 9, 90
Husser, T. O., Wende-von Berg, S., Dreizler, S., et al. 2013, A&A, 553, A6
Jenkins, J. M., Twicken, J. D., McCauliff, S., et al. 2016, Proc. SPIE, 9913, 99133E
Johnson, J. A., Petigura, E. A., Fulton, B. J., et al. 2017, AJ, 154, 108
Kane, S. R., Bean, J. L., Campante, T. L., et al. 2021, PASP, 133, 014402
Kovács, G., Zucker, S., & Mazeh, T. 2002, A&A, 391, 369
Lacedelli, G., Wilson, T. G., Malavolta, L., et al. 2022, MNRAS, 511, 4551
Lallement, R., Babusiaux, C., Vergely, J. L., et al. 2019, A&A, 625, A135
Lightkurve Collaboration, Cardoso, J. V. d. M. A., Hedges, C., et al. 2018, Lightkurve: Kepler and TESS time series analysis in Python, Astrophysics Source Code Library, ascl:1812.013
Lopez, E. D., & Fortney, J. J. 2013, ApJ, 776, 2
Lubin, J., Van Zandt, J., Holcomb, R., et al. 2022, AJ, 163, 101
Lucy, L. B., & Sweeney, M. A. 1971, AJ, 76, 544
MacDougall, M. G., Petigura, E. A., Angelo, I., et al. 2021, AJ, 162, 265
MacDougall, M. G., Petigura, E. A., Fetherolf, T., et al. 2022, AJ, 164, 97
Magliano, C., Kostov, V., Cacciapuoti, L., et al. 2023, MNRAS, 521, 3749
Mandel, K., & Agol, E. 2002, ApJL, 580, L171
Mann, A. W., Dupuy, T., Kraus, A. L., et al. 2019, ApJ, 871, 63
Mazeh, T., Holczer, T., & Faigler, S. 2016, A&A, 589, A75
McKinney, W. 2010, in Proc. 9th Python in Science Conference, Vol. 445, ed. S. van der Walt & J. Millman (Austin, TX: SciPy), 56
NASA Exoplanet Archive 2022, TESS Objects of Interest, vVersion: 2022-08-02, NExScI-Caltech/IPAC, doi:10.26134/ExoFOP3

Oh, M., & Berger, J. 1993, JASA, 88, 450
Osborn, H. P., Bonfanti, A., Gandolfi, D., et al. 2022, A&A, 664, A156
Owen, J. E., & Wu, Y. 2013, ApJ, 775, 105
Patel, J. A., & Espinoza, N. 2022, AJ, 163, 228
Petigura, E. A. 2015, PhD thesis, Univ. California, Berkeley
Petigura, E. A. 2020, AJ, 160, 89
Petigura, E. A., Howard, A. W., Marcy, G. W., et al. 2017a, AJ, 154, 107
Petigura, E. A., Rogers, J. G., Isaacson, H., et al. 2022, AJ, 163, 179
Petigura, E. A., Sinukoff, E., Lopez, E. D., et al. 2017b, AJ, 153, 142
Ricker, G. R., Winn, J. N., Vanderspek, R., et al. 2015, JATIS, 1, 014003
Rubenzahl, R. A., Dai, F., Howard, A. W., et al. 2021, AJ, 161, 119
Salvatier, J., Wiecki, T. V., & Fonnesbeck, C. 2016, PyMC3: Python
    probabilistic programming framework, Astrophysics Source Code Library,
    ascl:1610.016
Scarsdale, N., Murphy, J. M. A., Batalha, N. M., et al. 2021, AJ, 162, 215
Skrutskie, M. F., Cutri, R. M., Stiening, R., et al. 2006, AJ, 131, 1163
Smith, J. C., Stumpe, M. C., Van Cleve, J. E., et al. 2012, PASP, 124, 1000
Stassun, K. G., Oelkers, R. J., Pepper, J., et al. 2018, AJ, 156, 102
Stassun, K. G., Oelkers, R. J., Paegert, M., et al. 2019, AJ, 158, 138
Stumpe, M. C., Smith, J. C., Catanzarite, J. H., et al. 2014, PASP, 126, 100
Stumpe, M. C., Smith, J. C., Van Cleve, J. E., et al. 2012, PASP, 124, 985
Tayar, J., Claytor, Z. R., Huber, D., & van Saders, J. 2022, ApJ, 927, 31
Teske, J., Wang, S. X., Wolfgang, A., et al. 2021, ApJS, 256, 33
The Theano Development Team, Al-Rfou, R., Alain, G., et al. 2016,
    arXiv:1605.02688
Turtelboom, E. V., Weiss, L. M., Dressing, C. D., et al. 2022, AJ, 163, 293
Van Eylen, V., Agentoft, C., Lundkvist, M. S., et al. 2018, MNRAS, 479,
    4786
Van Eylen, V., Albrecht, S., Huang, X., et al. 2019, AJ, 157, 61
Van Zandt, J. E., Petigura, E. A., MacDougall, M., et al. 2023, AJ, 165, 60
Virtanen, P., Gommers, R., Oliphant, T. E., et al. 2020, NatMe, 17, 261
Vogt, S. S., Allen, S. L., Bigelow, B. C., et al. 1994, Proc. SPIE, 2198, 362
Weiss, L. M., Dai, F., Huber, D., et al. 2021, AJ, 161, 56
Winn, J. N. 2010, arXiv:1001.2010
Yee, S. W., Petigura, E. A., & von Braun, K. 2017, ApJ, 836, 77
Yee, S. W., Winn, J. N., Hartman, J. D., et al. 2022, AJ, 164, 70